Melting Phase Equilibria from 4 to 7 GPa in the System CaO-MgO-Al2O3-SiO2-CO2, the Persistence of the "Ledge" in Carbonated Basalt with Excess Silica, and the Most Likely Limits on the Depths of Termination of Carbon Cycle at Subduction Zones

Shantanu Keshav, Tahar Hammouda, Gudmundur H Gudfinnsson

OXFORD

Journal of Petrology, 2022, **63**, 1–27
https://doi.org/10.1093/petrology/egac069
Original Manuscript

Melting Phase Equilibria from 4 to 7 GPa in the System CaO-MgO-Al_2O_3-SiO_2-CO_2, the Persistence of the "Ledge" in Carbonated Basalt with Excess Silica, and the Most Likely Limits on the Depths of Termination of Carbon Cycle at Subduction Zones

Shantanu Keshav[1,2,*], Tahar Hammouda[3] and Gudmundur H. Gudfinnsson[1,4]

[1]Bayerisches Geoinstitut, Universität Bayreuth, Bayreuth, Germany
[2]Thapar School of Liberal Arts and Sciences, Thapar Institute of Engineering & Technology, Patiala, Punjab, India
[3]Université Clermont Auvergne, Centre Nationale de la Recherche Scientifique, Institut de Recherche Développement, Observatoire de Physique du Globe, Laboratoire Magmas et Volcans, F-63000 Clermont-Ferrand, France
[4]NordVulk, Institute of Earth Sciences, University of Iceland, Reykjavik, Iceland

*Corresponding author: Email: choteegai@gmail.com

Abstract

Melting phase relations involving model carbonated basalt with excess silica were studied in experiments over the pressure range of 4–7 GPa in the system CaO-MgO-Al_2O_3-SiO_2-CO_2 to determine if there is a sharp decrease in the melting temperatures along the transition from carbon dioxide vapor (vapor) to dolomite. The phase assemblages of clinopyroxene + garnet + coesite + vapor + carbon dioxide-bearing silicate liquid (silicate liquid) and clinopyroxene + garnet + coesite + dolomite + carbonate liquid, exist over 4–5 and 5.8–7 GPa, respectively. These two distinct phase assemblages form the two, vapor + silicate liquid and dolomite + carbonate liquid-bearing divariant surfaces. The dissolved carbon dioxide and the molar calcium number [Ca# 100^*(Ca/Ca + Mg)] of the silicate and carbonate liquids are approximately 4–8 wt% and between 50–55 and 35–40 wt% and 69–71, respectively. The compositions of phases vary little, implying minimal topography along the two surfaces, and the temperatures rise linearly along the silicate liquid-bearing divariant surface over 4–5 GPa. Between 5.2 and 5.6 GPa, however, the temperatures decrease precipitously by ~200–250°C and, along with this steep decline, the liquid changes from silicate to carbonate, with the rest of the phase assemblage of clinopyroxene + garnet + coesite + vapor, persisting. Hence, and this is important to emphasize, this liquid, coexisting with vapor, is carbonate in composition in the absence of dolomite. Isobaric invariance, at 5.4 GPa/1250°C, 5.6 GPa/1150°C, and 5.8 GPa/1100°C, consists of the six-phase assemblage of clinopyroxene + garnet + coesite + vapor + dolomite + carbonate liquid. Melting phase relations are thus univariant, and correspond to that of a solidus 'ledge', i.e. with a negative Clapeyron slope, in this part of the composition space. The melting reaction along the ledge is clinopyroxene + vapor = garnet + coesite + dolomite + carbonate liquid, and the ledge separates the two divariant surfaces. The Ca# of the coexisting carbonate liquid and dolomite here are opposite to those of the carbonate liquid and dolomite on the calcite-magnesite join at similar pressures as in this study. This is most likely a consequence of the combined effects of (a) observations from experiments and theory that the fusion curve of calcite starts to diverge from that of magnesite toward lower temperatures at pressures in excess of ~5 GPa, and (b) the pressure, where ultrabasic silicate–carbonate (~2.5–3 GPa) and excess-silica carbonate-basalt (>4 GPa, as inhere) systems undergo carbonation. These, in turn, cause the liquid and dolomite in experiments here to become more calcic and more magnesian than observed in experiments on the calcite-magnesite join. The solidus ledge, here, has a profound effect because the most plausible modern-day model ocean crust subduction zone geotherms in Earth will, in all likelihood, intersect it and cause fusion of dolomite, thereby, in effect, liberating all carbon from what once was a carbonate-basalt mixture. Thereafter, little exists to suggest that there is anything 'deep' to the carbon cycle, through recycling, with most of it likely confined to less than ~200 km in Earth.

Keywords: carbonatite, eclogite, subduction, phase equilibria, CMAS-CO2, CMAS, solidus, peridotite, basalt, vapor, carbonate, carbon

INTRODUCTION

The flux of carbon dioxide (CO_2) at subduction zone settings has been estimated to be similar to that at ocean spreading centers (ocean ridges), and it appears that ~80% of the CO_2 released in arc volcanism is derived from the subducted slab (Marty & Tolstikhin, 1998). Significantly more carbon, however, appears to be subducted than is released (e.g. Bebout, 1995; but also see Kelemen & Manning, 2015, and Hirschmann, 2018, and Plank & Manning, 2019), suggesting its subduction to depths in Earth beyond the source/s of arc silicate liquids (magmas/melts). Carbonate minerals may enter subduction zones incorporated in marine sediments and in hydrothermally altered ocean basalt, crust gabbro, and peridotite. The average CO_2 content of the marine sediment entering subduction zones has been estimated at 3 wt% (Plank & Langmuir, 1998), and the average CO_2 content of the sea-floor altered ocean ridge basalt is over 2.5–2.95 wt%

Received: August 30, 2021. **Revised:** June 20, 2022. **Accepted:** July 3, 2022

(Staudigel *et al.*, 1989; Coogan & Gillis, 2013; Coogan & Dosso, 2015). The CO_2 in the altered ocean crust is incorporated through precipitation of calcium (Ca), magnesium (Mg), and carbonate from seawater, chemicals and compounds, whose concentrations decrease with depth in the crustal section of the subducting ocean slab (Alt & Teagle, 1999). The main carbonate minerals entering the subduction zones, originally on the seafloor, are Ca,Mg-carbonates: calcite [$CaCO_3$] and dolomite [$CaMg(CO_3)_2$].

Indications for 'deep' subduction of carbonates come from the field exposures of ultrahigh pressure metamorphic rocks (e.g. Ogasawara *et al.*, 2000; Zhu & Ogasawara, 2002), in which, among other paragenesis, crystalline carbonates have been found coexisting with high-pressure phases, coesite (e.g. Zhang & Liou, 1996) and diamond (Ogasawara *et al.*, 2000). Most recently, the idea that partial fusion of carbonate–silicate mixtures (carbonate-basalt, wherein basalt could be either silica-normative tholeiite (favored), or possibly olivine-normative tholeiite) may have created some 'deep diamonds' (>300 km in Earth) and the inclusions they host has appeared in literature in various guises (e.g. Walter *et al.*, 2008; Shirey *et al.*, 2013; Thomson *et al.*, 2016). In this scenario, such diamonds and their inclusions are precipitates from liquids, carbonate in overall composition, are generated by partial fusion of the carbonate-basalt mixtures in subcontinental mantle at 'moderately great' depths (again, >300 km in Earth). Although hypothesized that such mixtures were transported to such depths through recycling at subduction zones, the *original* subducted basalt compositions of erupted tholeiite, at spreading centers, had largely been preserved (e.g. Stachel *et al.*, 2004; also see Thomson *et al.*, 2016), other than the addition of with carbonates (from the seafloor). Thereafter, crystalline carbonate greatly reduces the fusion temperatures of the carbonate-basalt mixture at conditions prevailing at depths of >300 km, because crystalline carbonate melts at much lower temperatures than the basaltic components in the mixture (e.g. Thomson *et al.*, 2016).

All the same, crystalline carbonates likely play a vital role toward genesis of liquids, such as, carbonatites, kimberlites, and melilitites (Canil & Scarfe, 1990; Dalton & Presnall, 1998a, 1998b; Gudfinnsson & Presnall, 2005), which are found almost exclusively in continents. Thus, altogether, carbonates and carbonate–silicate mixtures, and their expression/s in various forms, might constitute part of the *entire*, and the in-vogue, carbon cycle in Earth (*biotic processes*, excluded).

This work on melting phase relations involving model carbonated basalt with excess silica in the system CaO-MgO-Al_2O_3-SiO_2-CO_2 (CMAS-CO_2), over the pressure range of 4–7 GPa, is derived almost entirely on the basis of four published (Hammouda, 2003; Dasgupta *et al.*, 2004; Luth, 2006; Thomson *et al.*, 2016), and two presented papers (Shirasaka & Takahashi, 2003, International Kimberlite Conference, Vancouver, Canada; Luth, 2009, Peter J. Wyllie session organized by Hans Keppler, Yaoling Niu, Edward Stolper, and Marjorie Wilson, Goldschmidt Conference, 2009, Davos, Switzerland). On the basis of chemography, Thomson *et al.* (2016) recently suggested that the dominant carbonate-basalt mixture entering Earth's subduction zones is likely to be of silica-normative type, making it possible, in principle, to tie their experimental study with experimental studies by Hammouda (2003) and Shirasaka & Takahashi (2003), wherein starting compositions were silica-normative natural/multicomponent carbonate-basalt mixtures.

Crucially, then, phase relations reported here are equivalent to melting of silica-normative carbonate-basalt mixtures in natural/multicomponent systems (e.g. Hammouda, 2003). As such, melting phase relations in model systems provide useful anchor to which studies involving more complex compositions can be tied. This is because melting phase relations in natural/multicomponent systems, which are inherently high-variance systems, can possibly be better understood by utilizing model systems, such as in CMAS-CO_2 here, wherein variance can be controlled, without rigor being compromised. This, in turn, makes melting phase relations more tractable, than might be the case in natural/multicomponent systems.

On the basis of experimentally determined high-pressure melting phase relations of natural/multicomponent (i.e. components more than in CMAS-CO_2) silica-normative carbonated basalt (broadly defined as silica-normative carbonated eclogite), Hammouda (2003) concluded that the 'deep' carbon cycle, through recycling of carbon at subduction zones, is most likely confined to the top 300 km. Termination of this cycle, at approximately such depths, occurs because model geotherms at subduction zones intersect the fusion curve of the investigated carbonated basalt. And this intersection happens so as to cause melting of dolomite in the bulk mixture, thereby liberating carbon from it (dolomite being more fusible than calcite and magnesite, which are refractory at said conditions). This partial fusion primarily happens because model subduction zone geotherms coincide with the part of the fusion curve of the investigated carbonated basalt that has a steep negative Clapeyron slope over ~5–6 GPa (~150–190 km in Earth). This sudden and steep decline of the fusion curve is sometimes called the solidus 'ledge'. This ledge was first reported, and is quite possibly the most prominent feature in the solidus topology of model and multicomponent carbonated peridotite (see Luth, 2006). Nonetheless, once this partial fusion happens, carbon from the dolomite becomes part of the liquid, making the initial carbonate-basalt mixture virtually free of it. From hereafter, there is nothing deep to Earth's carbon cycle because carbon is no longer *stored* in the dolomite. Further fusion of the carbonate-free silicate is prevented because its melting temperature is higher than the initial carbonate–silicate mixture. Similarly, the form of experimentally determined high-pressure fusion curve of multicomponent silica-normative carbonated basalt starting composition used by Shirasaka & Takahashi (2003) is identical to that reported by Hammouda (2003). The only difference is that the fusion curve, including the ledge, in the former study is shifted to slightly lower pressures, by about 0.6–0.8 GPa, than reported by Hammouda (2003; see Fig. 10 in Hammouda & Keshav, 2015). In both Hammouda and Shirasaka & Takahashi, the solidus at pressures greater than the ledge coasts almost isothermally after about 6 and 8 GPa, respectively.

On the other hand, Dasgupta *et al.* (2004), on the basis of the experimentally determined high-pressure melting phase relations of multicomponent silica-deficient (norm) carbonated basalt starting composition, subscribed to the view that the carbon cycle, through subduction, prevailed to depths greater than >200 km. This happens because model subduction zone geotherms do not intersect the melting curve of the studied carbonated basalt, whereby melting of crystalline carbonate in the overall mixture is prevented. Therefore, if melting does not happen, then subduction of carbon continues unhindered whereby carbon can be at 'great depths'. The fusion curve of the carbonated basalt reported by Dasgupta *et al.* (2004) has a very different form (see Fig. 17 in Luth, 2006; also see Schettino & Poli, 2020) than the fusion curves reported by both Hammouda (2003) and Shirasaka & Takahashi (2003). (On as to how the starting carbonated basalt composition by Dasgupta *et al.*, 2004 was 'better' than used by Hammouda, 2003, reader is referred to the former study.) Nonetheless, the

carbonate-free starting silicate composition, a clinopyroxene (cpx)-garnet cumulate-from-liquid xenolith specimen from Salt Lake Crater, Hawaii, used by Dasgupta *et al.* (2004) is fairly enriched in magnesia compared with either the altered (Kelley *et al.*, 2003) or fresh ocean ridge tholeiite (Gale *et al.*, 2013). Therefore, in Dasgupta *et al.* (2004), both (a) the form of the solidus and (b) the absence of the ledge possibly have their roots in the chemistry of the starting material, which, being fairly magnesian, is silica-deficient (i.e. forsterite (olivine)-normative). Indeed, from the shape of the reported solidus, the ledge, if present, is most likely somewhere between 2 and 3 GPa, and hence might resemble the ledge in carbonated peridotite over these pressures (see Hammouda & Keshav, 2015). Likewise, Yaxley & Brey (2004) reported experimentally determined high-pressure melting phase relations of multicomponent silica-deficient carbonated basalt, and the forms of solidus curves of the investigated bulk compositions are very different from those in the aforementioned studies (see Fig. 17 in Luth, 2006).

Perhaps interested by the various forms of the solidi of the starting carbonated basalts reported up until the year 2006, Luth (2006) reduced melting phase relations of all such to the most fundamental system, diopside-CO_2 (diopside, $CaMgSi_2O_6$), since diopside (cpx) is one phase that is common to all studies. (In the system diopside-CO_2, the bulk composition is silica-normative.) In this system, melting temperatures initially rose from 1 to ~3 GPa, but from then and to 8 GPa they gradually declined by about ~200–250°C, with the lowest melting temperature seen at 8 GPa. In other words, unlike in Hammouda (2003) and Shirasaka & Takahashi (2003), the steep ledge is absent even though the starting composition in diopside-CO_2 is silica-normative, and coesite is present in the experiments. Gradually increasing solubility of lime (CaO) and CO_2 in the liquid, with increasing pressure from 3 to ~5 GPa, was cited as cause for the observed melting curve (Luth, 2006). Also, unlike in Hammouda (2003) and Shirasaka & Takahashi (2003), (a) the melting curve in diopside-CO_2, after it starts to decline, does not regain its positive fusion slope up to at least 8 GPa (see Figs 3 and 13 in Luth, 2006), and (b) appearance of dolomite at the solidus at ~5.5 GPa does not help to change the course of the melting curve from ~3 to 8 GPa, either.

In the paper presented at the 2009 Goldschmidt Conference, Luth remarked that the different high-pressure melting behaviors of the various carbonated basalts could possibly be understood by using chemography and projecting (from CO_2) these carbonate-basalt starting compositions in CMAS. Hence, for example, it is probably because the starting compositions used by Dasgupta *et al.* (2004) and Yaxley & Brey (2004) are silica-undersaturated, with respect to pyroxene-garnet ($CaSiO_3$-$MgSiO_3$-Al_2O_3) plane in CMAS, that the ledge is absent in these two studies.

Luth in 2009 also presented new experimental data on the high-pressure melting behavior of model carbonated basalt in two sub-systems in CMAS-CO_2, (a) the high-pressure melting behavior of the specific phase assemblage of clinopyroxene + garnet + vapor was indistinguishable from that in the system diopside-CO_2 (Luth, 2006). That is to say, that melting in both systems has 'gentle, negative fusion curves' after their initial positive Clapeyron fusion slopes; (b) the solidus topology with the specific phase assemblage of clinopyroxene + garnet + coesite + vapor (± solid carbonate (SC/sc)), on the other hand, was very similar to that of the multicomponent silica-saturated carbonated basalt (Hammouda, 2003), i.e. a proper ledge was present, but the melting curve in this particular sub-system—by way of lacking other components (e.g. sodium, potassium)—was shifted to higher temperatures than reported for the multicomponent silica-saturated carbonated basalt by Hammouda (2003). (Although Luth does not report the pressure range in the presented paper, it is assumed here that it is somewhere between 3 and 8 GPa.)

On these bases, it is reasonable to conclude, then, that when carbonate-basalt starting compositions are either silica-normative or experiments have free silica/coesite, primary vapor is likely to be stable to greater pressures along the high-pressure solidi of such mixtures than might otherwise be the case (e.g. carbonated peridotite; Dalton & Presnall, 1998a; Hammouda *et al.*, 2021). This, in turn, means that vapor to SC transition along the high-pressure solidi of such carbonate-basalt mixtures would also occur at higher pressures than, say, in carbonated peridotite.

The recent work by Thomson *et al.* (2016) on the high-pressure melting of silica-saturated multicomponent carbonated basalt merits note in the following manner:

(a) declining solidus temperatures, either gradually or by way of a steep ledge, are not observed over the pressure range of approximately 3–7 GPa, even though the investigated starting composition is on the silica-rich (and is hence, silica-normative) side of plane pyroxene-garnet in CMAS, and all three phases, vapor, dolomite, and coesite are present in the experiments; at least two other studies, by Hammouda (2003) and Shirasaka & Takahashi (2003), have independently documented the ledge in this part of the composition space that the silica-excess carbonate-basalt mixtures encompasses.

(b) it is suggested that their solidus data are consistent with boundary curve, cpx + vapor = dolomite + coesite (Luth, 1995). This, in all likelihood, is incorrect because once this univariant reaction gets terminated by its intersection with the vapor-bearing solidus, the subsequent dolomite-only (plus silicate) phase assemblage, at the solidus, cannot exist at temperatures higher than the prior vapor- and silicate liquid-bearing phase assemblage (e.g. Hammouda, 2003). As stated before, this remarkable change in melting systematics, ascribed to vapor-crystalline carbonate transition, is not only limited to systems under immediate consideration (e.g. Hammouda, 2003; Shirasaka & Takahashi, 2003), but also possibly the most prominent feature of the solidus topology of carbonated peridotite over 2–3 GPa. For example, once the relevant carbonation reaction intersects the vapor-only fusion curve in carbonated peridotite where free silica is not involved, the resulting dolomite-only phase assemblage is always at lower temperatures than the prior vapor-only phase assemblage (Dalton & Presnall, 1998a; see Luth, 2006, and Hammouda *et al.*, 2021). (It is to be remembered that vapor and dolomite can, and do, coexist under a defined set of conditions, as, for example, in model carbonated peridotite in CMAS-CO_2; Dalton & Presnall, 1998a.);

(c) it is also suggested that magnesite, ideally, would not be the stable subsolidus/solidus crystalline carbonate phase in the experiments reported by Hammouda (2003) and Dasgupta *et al.* (2004) because of the kinds of the starting carbonate-basalt compositions used in these studies, and yet—the opposite is observed—Hammouda (2003) and Dasgupta *et al.* (2004) do report magnesite in their respective experiments. (This argument by Thomson *et al.* on the absence of magnesite is also extendable to the silica-normative carbonate-basalt starting composition used by Shirasaka &Takahashi (2003), wherein both aragonite and magnesite are reported.) In fact, the very specific silica-normative carbonate-basalt starting composition used by Thomson *et al.* ensures the absence of calcite/aragonite, and that magnesite would be the stable crystalline carbonate

subsolidus/solidus phase in the obtained runs, once dolomite has disappeared from the phase assemblage;
(d) between ~13 and ~6 GPa, the solidus of the investigated starting composition has a negative Clapeyron slope, and between 16 and 21 GPa, the solidus is almost isothermal.
(e) the densest experimental coverage is at the 21 GPa datum, while it could have been had over the pressure range of 13–16 GPa, and this is because this is the pressure range over which the Clapeyron slope starts to become negative, from its initial, positive slope over, say, 7.5–12.5 GPa, eventually achieving its maximum trough at about 17 GPa.

Consequences of this 'second' solidus ledge ('second', adopted here), between 13 and 16 GPa, instead of the 'more' familiar (~ 4–6 GPa, as in the studies byHammouda, 2003 ; Shirasaka & Takahashi, 2003), could be quite important. For example, the carbon cycle, through subduction, terminates at depths which are less than 300 km in Earth (e.g. Hammouda, 2003), in Earth's Transition Zone (Thomson *et al.*), or continues undisturbed at depths greater than 200 km in Earth (Dasgupta *et al.*, 2004). According to Thomson *et al.*, the fusion curve in their study, with its negative Clapeyron slope over 13–16 GPa, may also imply that some deep diamonds and their guest inclusions, interpreted to be precipitates from carbonate melts from partial fusion of subducted carbonate-basalt mixture (e.g. Walter *et al.*, 2008), are limited to depths of about 300–600 km in Earth. These differences from various previous works (save Yaxley & Brey, 2004) are shown in a projection in Fig. 4.

Therefore, on these bases, and for possible consequences primarily toward phase equilibria, generation of liquid and its expression in Earth and what might it mean for recovered specimens (magmas/melts/solids) from Earth, and the ∗continuing∗ interest in 'deep-Earth carbon cycle', the attending in this study are as follows:

(a) the form of the fusion curve of carbonated basalt over the pressure range of 4–7 GPa (~ 120–200 km in Earth) in the system CMAS-CO_2;
(b) liquid compositions, vital, because of their dramatic change reported previously (e.g. Hammouda, 2003), but more importantly in their absence, one is bound to ask, 'what is the point?';
(c) clarification, if that, of the high-pressure fusion curves reported for multicomponent silica-saturated carbonated basalt (Hammouda, 2003; Shirasaka & Takahashi, 2003); and
(d) purely from a model system perspective, whether or not high-pressure melting phase equilibria of simplified carbonated basalt have the capacity to say anything meaningful toward this 'deep-Earth carbon cycle'.

WORKING METHOD FOR THIS STUDY

Except for the data presented by Luth in the paper in 2009, melting behavior of (any) carbonate-basalt in model system/s is virtually unknown. Therefore, in order to be able to have some form of working direction for experiments in the present study in CMAS-CO_2, melting phase relations in the tholeiite (forsterite-anorthite-diopside-quartz; fo-an-di-qz) part of the basalt tetrahedron in the system CMAS at 3 GPa (Milholland & Presnall, 1998) initially served as guides.

While with the understanding that there is conjecture, the starting point, for carbonated basalt in this study, is isobaric invariance at 3 GPa and 1460°C in fo-an-di-qz (see Figs 9 and 13 and Table 7 in Milholland & Presnall, 1998), with orthopyroxene (opx) + cpx + garnet + quartz coexisting with liquid (Fig. 1). With falling temperature from this invariance, another isobaric invariance at 3 GPa and 1400°C, comprised of cpx + garnet + quartz + kyanite + liquid, is encountered. It follows, then, that isobaric univariance, cpx + garnet + quartz + liquid (model silica-eclogite?) is bounded by the two isobaric invariant points at 1460 and 1400°C. Increasing pressure, which causes quartz-coesite transition from the subsolidus (e.g. Bohlen & Boettcher, 1982; Bose & Ganguly, 1995), makes the phase assemblage consisting of opx + cpx + garnet + coesite + liquid stable to pressures greater than 3 GPa. To reiterate, then, opx-bearing (and kyanite-absent (ky)) phase assemblage occurs along pressure–temperature univariance, A-B (in solid, Fig. 1, coesite is 'coe') in fo-an-di-qz and, along A-B, a pressure–temperature invariant point, consisting of opx + cpx + garnet + quartz + coesite + liquid, exists.

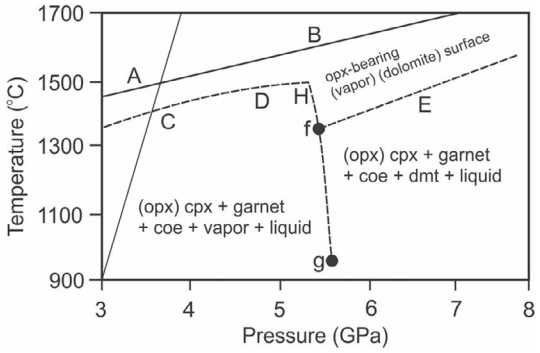

Figure 1. Pressure–temperature diagram showing the strategy adopted in this study. For details, see 'Working Method…' in the main text. The solid, fine line represents the transition from quartz (low-pressure side of 'C') to coesite (high-pressure side of 'A'), and has been drawn after Bose & Ganguly (1995). Notations are as follows: cpx, clinopyroxene; coe and cst are used interchangeably for coesite; dmt is dolomite and, from here on, is also shown/written as SC/sc; and opx is orthopyroxene, and its absence is shown in parentheses, (opx).

With CO_2 added to the tholeiite in fo-an-di-qz, and in the absence of pure alumina-silicate (e.g. kyanite, Al_2SiO_5) or pure alumina (e.g. corundum, Al_2O_3) crystalline phases, the opx + cpx + garnet + quartz (coesite) + liquid univariance (A-B, in fo-an-di-qz; Fig. 1) becomes a divariant surface, while the invariance, with quartz and coesite between A-B, splits into a univariant curve. (For the purposes here, quartz-coesite transition along A-B is ignored.) Temperatures fall from univariant A-B because of some solubility of CO_2 in the liquid. When the decrease in temperatures continues, the divariant surface, with opx + cpx + garnet + coesite + liquid, is terminated at some finite pressure lower than about 5.5 GPa by vapor saturation (in natural systems, from, Hammouda, 2003 and Shirasaka & Takahashi, 2003; both studies in opx-absent systems), making melting phase relations pressure–temperature univariant. When this happens, the phase assemblage consists of opx + cpx + garnet + quartz (coesite) + vapor + liquid (liquid is CO_2-bearing; along C-D-H (and perhaps its metastable parts), long-dashed; Fig. 1), and every liquid below A-B will contain carbon dioxide. In other words, the univariant boundary curves, approximated as A-B-C-D-H, partially contain this divariant surface that has opx, and liquid with some dissolved CO_2 in it. Now, with further falling temperature from univariant C-D-H, opx is lost and, instead, the assemblage is cpx + garnet + coesite + vapor + liquid. Therefore, the phase assemblage, cpx + garnet + quartz (coesite) + liquid in CMAS, is divariant, still, in CMAS-CO_2, only with free vapor.

This variance means that the vapor-bearing (and opx-absent (opx); opx-absent is shown in parentheses) divariant surface will terminate by some other mechanism at its lower-temperature reaches than is the case for model tholeiite in fo-an-di-qz in CMAS.

Getting guidance from Hammouda (2003) and Shirasaka & Takahashi (2003), the transition from vapor to SC (e.g. dolomite) happens somewhere between 4 and 6 GPa. While before this transition, the solidus in these respective studies has positive Clapeyron slope, after it, the solidus has negative Clapeyron slope (the ledge). This change is a very prominent feature in the solidus topology in both these studies, and most likely happens because carbonation of type, cpx + vapor = dolomite + coesite (Luth, 1995), occurs, and also because dolomite has lower fusion temperature than the silicate (basalt) with which it coexists. Likewise, if opx-containing C-D-H is followed, the transition from vapor to dolomite could happen somewhere between 5 and 6 GPa in CMAS-CO_2 (but also from fo-di-an-qz), whereby C-D-H might devolve into the ledge. This scenario implies that C-D-H, will, at some point, make melting phase relations pressure–temperature invariant. At this invariance, 'f', because vapor and dolomite (dolomite is 'dmt'; Fig. 1) will coexist for the first time, the phase assemblage will consist of opx + cpx + garnet + coesite + vapor + dolomite + liquid.

It is important to emphasize here that the only place where opx will coexist with vapor, dolomite, and liquid is at the 'f' invariance. This further means that carbonation reaction, here will be of type, opx + cpx + vapor = garnet + coesite + dolomite, and hence will sit somewhere between that for the opx-absent 'basic' system, cpx + vapor = dolomite + coesite (Luth, 1995), and carbonated peridotite, forsterite + cpx + vapor = opx + garnet + dolomite (Dalton & Presnall, 1998a). The reaction involving opx and silica has previously been of type, cpx + vapor = opx + dolomite + silica in CMS-CO_2 (Schrauder & Navon, 1993, but see Wyllie *et al.*, 1983, and Knoche *et al.*, 1999), and is, then, not very different from that written here.

Univariant 'E' (long-dashed; Fig. 1) emanates from 'f', along which dolomite-bearing phase assemblage will exist. Although below E (and in the area contained in 'f-g-E') liquid is most likely of calciocarbonate composition, along it, things are probably different. For example, 'E' not only has (required) positive Clapeyron slope, but liquid here coexists with three very siliceous phases, opx, cpx, and coesite, plus free dolomite and garnet (also see Luth, 1995). Now, E comes into effect from (1) A-B in fo-an-di-qz and (2) the dolomite-bearing surface below it, but by virtue of bearing opx, and because the (conceived) ledge is before it, liquid composition, along it, is most likely to be of mixed calcic-magnesian carbonate type than below it, or, for that matter, even along 'f-g'. Also, as compared with the liquid along C-D-H, the liquid along E will have more carbon dioxide in it.

Along C-D-H (with silicate liquid), different things happen, however, because as it turns into 'f', liquid, just before, will most likely become carbonate in its composition. This is most likely correct because dolomite is about to appear as part of the phase assemblage according to the carbonation reaction written above. Due to this, (1) a singular situation may arise, whereby along C-D, opx and coesite, which are initially on the product and reactant sides, respectively, switch sides as liquid acquires its carbonate composition somewhere over the pressure–temperature distance, 'H-f' ('H' being singularity), and (2) along H-f, cpx and vapor, are on the reactant side. This scenario with liquid here is similar to what happens along the solidus ledge in model carbonated peridotite in CMS-CO_2 (Hammouda *et al.*, 2021) and CMAS-CO_2, whereby liquid is carbonate in its composition at about 2 GPa while dolomite first coexists with vapor at about 3 GPa. Therefore, for a relatively long (~1 GPa) pressure interval (2 to 3 GPa), liquid is of carbonate composition without dolomite, and that cpx and vapor are primary contributors melting and melt compositions along the ledge in carbonated peridotite (Novella *et al.*, 2014).

Along the construct, C-D-H, that is sketched from A-B in fo-an-di-qz and Hammouda (2003) and Shirasaka & Takahashi (2003), bulk compositions would be fairly different than those along 'H'f-g'. This is because along C-D-H liquid will contain less CO_2 dissolved in it, than along 'H-f'g', because along it, temperatures will decrease because of high concentrations of CO_2 in the liquid. This means that bulk compositions that may be used to understand melting phase relations along C-D-H will have less amount of CO_2 than along 'H-f'g', which lies at lower temperatures than the former, implying that bulk compositions along it would necessarily have to contain higher CO_2 than was the case along C-D-H. Similarly, in the area contained in 'f-g-E', bulk compositions also would have higher CO_2 than C-D-H, or even along 'E'.

That this invariance, 'f', exists, comes also from the observation that three divariant surfaces, vapor- and dolomite-bearing (both opx-absent), and that bounded by A-B-C-D-H-E (opx-bearing), can be seen to coalesce. From this invariance, it follows, then, that seven univariant curves emanate, which are, with the absent phase shown in parentheses, (1) (opx) cpx + garnet + coesite + vapor + dolomite + liquid (between 'f-g'; Fig. 1); (2) (cpx) opx + garnet + coesite + vapor + dolomite + liquid; (3) (garnet) opx + cpx + coesite + vapor + dolomite + liquid; (4) (coesite) opx + cpx + garnet + vapor + dolomite + liquid; (5) (vapor) opx + cpx + garnet + coesite + dolomite + liquid ('E'; Fig. 1); (6) (dolomite) opx + cpx + garnet + coesite + vapor + liquid (curve C-D-H, and its slight traverse toward 'f', but getting terminated before it, Fig. 1), and (7) (liquid) opx + cpx + garnet + coesite + vapor + dolomite (carbonation reaction involving opx).

Due to aluminous opx and garnet in this study, the following are probably important: (1) the intersection of carbonation, opx + cpx + vapor = garnet + coesite + dolomite, with vapor-, opx-, and dolomite-bearing univariant solidi, contained in C-D-H-E, makes everything invariant (Fig. 1, 'f', again); (2) thus, if the starting point is from the primary volume of opx in fo-an-di-qz, carbonation reaction would have to involve this phase to make cpx + garnet + coesite + vapor + dolomite + liquid (melting relations would be univariant when this phase assemblage becomes stable) as the final goal in experiments (somewhere along 'f-g'); (3) with opx, the carbonation reaction is still univariant but, because of it, vapor must be absent toward the high-pressure side of 'f-g' (along 'E'); (4) thus, geometry requires that, somewhere along C-D-f-E, there is, most likely, at least part of the ledge in the part of the composition space containing opx; (5) by removing opx from 'f', variance is gained, for example, toward 'g'. A consequence of all this might be that the carbonation reaction, that previously necessarily has to terminate at 'f', is now spread along a univariant curve in the absence of opx. This is the univariant reaction that most likely occurs along 'f-g'. (Purely in terms of variance, the depicted situation at 'f' is almost identical with carbonation reaction in model carbonated peridotite that has both forsterite and opx; Dalton & Presnall, 1998a.)

For the purposes of the present study, data along and around 'f-g', the (opx) univariant curve, are the most significant, for it contains model carbonated basalt that is saturated with free silica (coesite). Also, if melting phase relations in fo-an-di-qz (model tholeiite, Milholland & Presnall, 1998), and those reported by Hammouda (2003) and Shirasaka & Takahashi (2003) in

carbonate-basalt are correct, then, according to the construct, this (opx) curve becomes visible only when temperatures fall below the 'f' invariance. The (opx) curve, between 'f-g', also signifies that the vapor- and dolomite-bearing surfaces (Fig. 1), should somehow merge along it ('g' does not carry any geometric significance with it, and is shown only to aid describing the construct). Thus, in order to have better control on the topology than can be deduced from Fig. 1, one need determine, two, possibly three, univariant curves emanating from 'f', and the rest can be constructed on the basis of chemographic/algebraic schemes. Besides topology, hint on the ledge likely being present can also be had from following the chemistry of the liquid that exists with a pre-defined phase assemblage as a function of pressure. For example, over a relatively fairly tiny pressure distance, a liquid, initially containing, say, 5–8 wt% carbon dioxide in it, will, instead, find itself containing more than 30–35 wt% carbon dioxide.

As in fo-an-di-qz (e.g. Milholland & Presnall, 1998; Liu & Presnall, 2000), there are, in all likelihood, composition spaces in CMAS-CO_2 (carbonate-basalt) where kyanite, corundum, and possibly sapphirine ($Mg_2Al_4SiO_{10}$) will be stable volumes along with those considered here, but such are avoided here. These are avoided because the composition space is simply enormous and, therefore, some form of theoretic parameterization, most likely guided by experiments, might be needed to completely understand melting phase relations involving these latter phases in CMAS-CO_2. With this, it is also important to remember that the mere presence of crystalline phases such as free silica (quartz/coesite), corundum, kyanite, or sapphirine, in documented cpx-garnet-bearing specimens (e.g. garnet pyroxenite, or eclogite), recovered from kimberlites, melilitites, alkali basalts in continents/ocean settings, does not automatically imply that these necessarily would somehow have to be of recycled origin, i.e. of past ocean subduction. This is because crystal fractionation of tholeiite, say, over pressure range of 2–4 GPa, is a perfectly viable mechanism to produce such specimens, and hence such rocks are precipitates (cumulates) from magmas at fairly elevated pressures (e.g. Exley & Smith, 1983; Smyth *et al.*, 1989; Milholland & Presnall, 1998; Liu & Presnall, 2000). Yet, it is possibly because of the normative composition of erupted tholeiite, it is not unusual that some previous studies have investigated this part of the composition space in carbonate-basalt in natural systems (Hammouda, 2003; Shirasaka & Takahashi, 2003; Thomson *et al.*, 2016).

On these bases, but most importantly, to make it all tractable, the task here was to have experiments spanning the opx-absent surfaces ((opx); Fig. 1). From this, it stands to conceive that coexisting vapor and dolomite would provide controls on univariance along 'f-g', which might, following Luth (2009) and as outlined before, contain the ledge in this part of composition space.

METHODS

Here, 5 g each of starting compositions (Table 1) were prepared using fine powders of $CaCO_3$ (99.998% purity, Alfa Aesar®), MgO (99.997% purity, Alfa Aesar®), Al_2O_3 (99.998% purity, Alfa Aesar®), and SiO_2 (99.995% purity, Aldrich®) as mixtures of silicate glasses and crystalline magnesite (magnesite, $MgCO_3$, source of all CO_2 and some magnesia, MgO). The magnesite comes from Oberdorf, Austria (graciously supplied by Peter Ulmer, ETH Zürich), and has been used in a previous experimental study on carbonates (Buob *et al.*, 2006). On the bases of studies by Milholland & Presnall (1998), Hammouda (2003), and Shirasaka & Takahashi (2003), each starting mixture was prepared so as to yield considerable liquid coexisting with model carbonated basalt phase assemblage in experiments. A large proportion of liquid, coexisting with a defined set of phase assemblage (e.g. Fig. 1), also facilitates chemical equilibrium, and makes determination of its chemical composition, at very low melt fraction, using electron microprobe, possible.

Silicate portions, as glasses, of the bulk starting mixtures were prepared, first. Throughout, platinum (Pt) crucibles were employed that had not been previously used to contain/dry/fire, or fuse iron/sodium/potassium/chromium-bearing materials. Powders of $CaCO_3$ and MgO, Al_2O_3, and SiO_2, contained in their individual Pt crucibles were fired for 12 h at 350°C and 1200°C, respectively. The fired powders containing MgO, Al_2O_3, SiO_2 and $CaCO_3$ were mixed in their respective proportions, and were decarbonated in high-temperature furnace. Temperature of the furnace was raised gradually from 100°C to 600°C over 6 h, maintained at 600°C for 6 h, raised from 600°C to 1000°C over 6 h, and finally kept at 1000°C for about 10 h. Post this step, these portions were fused and made into silicate glass in high-temperature furnace at 1600°C for 4 h in Pt crucibles. To quench the silicate portions, these crucibles were taken out of the furnace and were partially immersed in ice-water bath in a glass beaker. The resulting glass was optically transparent.

Silicate glasses were prepared in quantity, which was in excess than required to make the bulk starting mixtures (i.e. silicate glasses + crystalline magnesite). This was done because, during initial testing of starting glasses, some portions of these were found cemented hard onto the inside walls of the Pt crucibles after quenching, and hence were very difficult to pry from them. Nonetheless, glasses were crushed and ground under ethanol in an agate mortar for about 1 h, and were re-melted and re-crushed and re-ground once more, followed by a third glassing-crushing-grinding cycle. In between each glassing-crushing-fine powdering step, these glasses were dried for about 1 h under infrared (IR) heat lamp. Finely ground crystalline magnesite from Oberdorf was first dried for approximately 2 h under IR lamp and was then fired for over 27 h over 200–250°C in air in Pt crucible. Finally, silicate glasses and magnesite were mixed in their appropriate proportions, ground in agate mortar under ethanol for 1 h, dried under IR lamp, ground and dried again, and the final contents stored in vacuum box furnace at about 200°C. All starting mixtures were prepared in identical manner.

High-pressure experiments from 4 to 7 GPa (Table 2) were performed with a traditional, uniaxial, split-sphere multianvil apparatus (MA6/8 module; Sumitomo 1200) installed at Bayerisches Geoinstitut (BGI, Bayreuth), Germany. Experiments were performed using Cr_2O_3-doped MgO (MgO-Cr_2O_3) pressure cells with edge lengths of 18 mm. Second-stage tungsten carbide (WC) anvils (32 mm edge lengths) with 11 mm truncated edge lengths were used, and this arrangement is labeled as 18/11-type (18/11) pressure-cell assembly (see Keppler & Frost, 2005). The 18-mm pressure cells at BGI consist of zirconia thermal insulators, dense 4-bore alumina (Al_2O_3) sleeves to house the thermocouple wires (see below), soft magnesia and alumina inserts, and lanthanum chromite ($LaCrO_3$) heaters, which are stepped to reduce temperature gradient in the capsule containing the starting mixture. In this type of assembly at BGI, molybdenum rings on either end of the pressure cells serve as electric contacts with the second-stage WC anvils. Pyrophyllite was used as gasket material in all experiments, and further details on the pressure cells used here can be found in Keppler & Frost (2005).

Table 1: Nominal composition (wt%) of starting mixtures in the system CaO-MgO-Al_2O_3-SiO_2-CO_2 (CMAS-CO_2) used in the present study

Mixture	CaO	MgO	Al_2O_3	SiO_2	CO_2[+]	Ca#[++]
CB - 1	15.95	13.68	14.67	44.63	11.07	45.44
CB - 4	13.72	12.38	13.41	46.77	13.72	44.18
CB - 9	13.46	10.99	11.66	47.57	16.33	46.66
CB - 10	29.30	15.60	6.20	25.10	23.80	57.27
CB - 6	28.40	15.20	7.01	28.50	20.90	57.12
CB - 13	29.70	13.60	6.78	29.30	20.60	60.83
CB – 19	27.07	13.73	6.59	23.99	28.60	58.74
CB – 22	24.03	11.42	6.53	24.15	33.84	60.05

[+]Added as crystalline magnesite, $MgCO_3$ (naturally occurring crystalline magnesite from Oberdorf, Austria; from Peter Ulmer, ETH Zürich) [++]Ca# is molar Ca/Ca+Mg*100 of the starting mixture (labeled 'mixture' in this table, or anywhere else in the presented work); starting mixture, mixture, and bulk composition are used interchangeably; Ca#/Ca-no./Ca no. carries the same meaning throughout.

Single-bore Pt metal (99.995% purity, Goodfellow®) tubing, measuring 1.4 mm in length and 1.2 mm and 1.6 mm in inner and outer diameter, respectively, was used as capsule material. Approximately 0.6–0.8 mg of the starting mix was loaded into Pt capsule that had previously been ultrasonically washed for ∼10 min in ethanol, annealed at 1000°C in air for ∼1 h, boiled for ∼10 min in dilute hydrochloric acid, fired at 1000°C for ∼10 min in air, sealed at one end by arc welding (capsule was triple-crimped at this stage), again ultrasonically washed in ethanol (for ∼10 min), and fired in air at 1000°C (for ∼30 min). After these steps, the capsule and starting mixture were dried for at least 12 h at 250°C, and kept in oven at 120°C right before assembling the pressure cell.

The 18-mm pressure cell, zirconia thermal insulator, $LaCrO_3$ heater, magnesia and alumina spacers, and alumina thermocouple sleeves were fired for 2 h in air at 1000°C in box furnace. Following this step, the other end of the triple-crimped Pt capsule with the starting mixture was welded shut, after which some weight loss amounting to about 0.01–0.03 mg of the entire Pt capsule was noticed. This loss might have been caused either by Pt metal volatilizing during the final welding, or by loss of CO_2 from the starting mixture. Capsules with mass loss equal to or more than 3% relative to the initial mass were discarded. After complete welding and gently flattening both ends, the final height and width dimensions of the Pt capsule were approximately between 1–1.1 mm and 1.1–1.2 mm, respectively.

Thick-walled Pt capsules were used so that the starting mixture was surrounded by lot of metal, and this supposedly results in smoothening of temperatures inside the capsule. Inside the pressure cell, a straight, cylindrical magnesia sleeve (fired for 2 h in air at 1000°C in box furnace) separated the capsule from the stepped $LaCrO_3$ heater. Spacers made of soft magnesia and alumina (fired for 2 h in air at 1000°C in box furnace) below the capsule were used to center it in the pressure cell. Temperatures were measured using type D (tungsten (W)-rhenium (Re); $W_{75}Re_{25}/W_{97}Re_3$) thermocouple wires (0.15 mm thick, Omega®), and these wires, encased in 4-bore alumina tube, were in direct contact with the Pt capsule, and there was no evidence of contamination of the thermocouple wires with the Pt capsule. The thermocouple wires encased in the 4-bore alumina sleeves were dried again at 120°C in air in box furnace. As the last step, the final, assembled pressure cell, inclusive of the capsule and alumina sleeve housing the thermocouple wires, was fired for about 10–11 h in air at 150°C. Temperatures reported in the manuscript are thermocouple readings and ignore the effect of pressure on the thermocouple emf. Following Nishihara *et al.* (2006), type D thermocouple wires themselves were coiled to house the thermocouple exiting the pressure cell. Experiments were brought to the target pressure at ∼1 GPa/h, heated at ∼100°C/min to the target temperature, and maintained to within ±5°C of the target temperature using Eurotherm controller.

After termination of the experiment, the Pt capsule was recovered from the pressure cell and was examined under a binocular microscope to ascertain if the W-Re thermocouple had pierced the Pt capsule—such was not the case. After this step, the Pt capsule was mounted longitudinally in Petropoxy-154 resin and ground and polished for optical and electron microprobe examination. As precaution, charges were polished without water and under oil on SiC grit (240–1000) paper were frequently washed ultrasonically in ethanol, and were polished again on SiC grit (1000) paper. In between polishing on SiC grit, it was found necessary to impregnate the Pt capsule with resin as was used for the initial mounting. Final polishing was done on felt (37–25 μm) using 3–0.25 μm diamond paste (Struers®).

Chemical analyses of phases (Tables 3–6) in experiments were performed at BGI by using a 5-spectrometer JEOL JXA-8200 Superprobe electron microprobe in wavelength-dispersive spectrometry mode with an accelerating voltage of 15 kV and 15 nA probe current (at the Faraday cup). Quenched liquid was analyzed using beam diameter of 15–20 μm and the beam diameter was 1 μm for crystalline phases, with a combination of diopside, enstatite, forsterite, and pyrope, as standards. Analyses were performed in fixed spot mode, and reduced using the ZAF correction scheme. Counting times for phases on peak and background for the four oxides, CaO, MgO, Al_2O_3, and SiO_2, were 30 and 15 s, respectively. The amount of CO_2 in quenched liquid and crystalline carbonate was estimated by difference. In calculating the matrix corrections for melt and crystalline carbonate, the program assumes that the oxide not being analyzed is CO_2.

Temperature gradient in the 18/11 pressure cell with sectioned $LaCrO_3$ heater and Pt capsule, as used for experiments here, was estimated by equilibrating a 1:1 mixture (generously supplied by Daniel Frost, Bayreuth) of synthetic end-member enstatite and diopside pyroxene compositions. This experiment, with enstatite and diopside contained in platinum, was run for approximately 39 h in 18/11-type pressure cell at 5 GPa and 1400°C, and temperatures in the Pt capsule were estimated from the Ca-Mg exchange between 35 adjacent enstatite and diopside pairs using the two-pyroxene solvus geothermometer of Gasparik (1990). Calculated pyroxene solvus temperatures vary by ±40–50°C in the capsule and are without systematic gradients from top-to-bottom and side-to-side (Fig. 2). This apparent temperature variation in the Pt capsule is of the same magnitude as the uncertainty in the thermometer proposed by Gasparik (1990). Hence, on this basis,

Table 2: Experimental conditions and results

Run	P (GPa)	T (°C)	Dur, h, min	M	Results/notes
47	4	1500	11	CB - 1	All molten
50	4	1450	15	CB - 1	All molten
37	4	1350	79	CB - 1	cpx + gt + cst + void + liq
26	4	1300	77	CB - 1	cpx + gt + cst + void + liq
21	4	1250	81	CB - 1	cpx + gt + cst + void + liq*
13	4	1200	85	CB - 1	gt + cst + void + liq
51‘	4.5	1600	9	CB - 4	All molten
56	4.5	1500	14	CB - 4	All molten
14	4.5	1400	74	CB - 4	cpx + gt + cst + void + liq
7	4.5	1350	80	CB - 4	cpx + gt + cst + void + liq
3	4.5	1300	74	CB - 4	cpx + gt + cst + void + liq
35	4.5	1250	82, 20	CB - 4	gt + cst + void + liq
54	5	1650	7, 30	CB - 9	All molten
58	5	1550	9	CB - 9	All molten
31	5	1450	69, 30	CB - 9	cpx + gt + cst + void + liq
29	5	1400	82	CB - 9	cpx + gt + cst + void + liq
39	5	1350	85	CB - 9	cpx + gt + cst + void + liq
15	5	1300	77	CB - 9	gt + cst + void + liq
114	5.2	1400	71	CB - 9	All molten
103	5.2	1300	73	CB - 22	cpx + gt + cst + void + liq
107	5.2	1250	82, 20	CB - 22	cpx + gt + cst + void + liq
96	5.4	1400	70, 25	CB - 9	All molten
97	5.4	1350	71, 30	CB - 9	All molten
122	5.4	1250	77, 40	CB - 19	cpx + gt + cst + void + sc + liq
111	5.4	1200	79, 10	CB - 22	cpx + gt + cst + void + liq
112	5.5	1150	74	CB - 22	cpx + gt + cst + void + liq
91	5.6	1300	68	CB - 19	All molten
129	5.6	1150	73	CB - 19	cpx + gt + cst + void + sc + liq
109	5.6	1100	78	CB - 22	cpx + gt + cst + void + liq
140	5.8	1300	69, 10	CB - 13	All molten
130	5.8	1200	72, 15	CB - 13	cpx + gt + cst + sc + liq
132	5.8	1150	75	CB - 13	cpx + gt + cst + sc + liq
147	5.8	1100	82, 10	CB- 19	cpx + gt + cst + void + sc + liq
67	6	1600	7	CB - 6	All molten
74	6	1550	41	CB - 6	All molten
62	6	1500	12	CB - 10	All molten
77	6	1400	56	CB - 10	All molten
76	6	1350	52	CB - 10	All molten
12	6	1200	85	CB - 6	cpx + gt + cst + sc + liq
23	6	1150	87, 40	CB - 6	cpx + gt + cst + sc + liq
17	6	1100	86	CB - 10	cpx + gt + cst + sc + liq
41	6	1050	83, 10	CB - 10	cpx + gt + cst + liq
60	7	1650	5	CB - 6	All molten
70	7	1600	6, 30	CB - 13	All molten
64	7	1500	13	CB - 13	All molten
66	7	1450	29	CB - 13	All molten
68	7	1400	31	CB - 6	All molten
81	7	1300	51	CB - 6	All molten
84	7	1250	77	CB - 13	All molten
5	7	1150	84	CB - 13	cpx + gt + cst + sc + liq
19	7	1100	91, 40	CB -13	cpx + gt + cst + sc + liq
8	7	1050	89	CB - 13	cpx + gt + cst + sc + liq
11	7	1000	89, 35	CB - 13	cpx + gt + cst + liq

Notes: P, pressure; T, temperature; cpx, clinopyroxene; gt, garnet; cst and coe are used interchangeably for coesite (free silica phase); M, starting mixture; liq, quenched liquid/liquid/melt/quenched melt. *Void space from gray-scale BSE image of capsule cross-section using imaging program of electron microprobe, and is coupled with mass-balance; void is interpreted as free vapor. **Unless otherwise noted, sc/SC, whenever mentioned, is solid carbonate (assigned to dolomite composition).

and to be conservative, this is the temperature uncertainty ascribed to the experimental temperatures reported in Tables 2–6.

Compositions of starting mixtures, CB - 1, CB - 4, and CB - 9, are shown in Fig. 3, in a projection (molar) from diopside [di] and [CO_2] onto the forsterite-calcium tschermak's-quartz (Fo-CaTs-Qz/fo-cats-qz) join (Herzberg & O'Hara, 1998); also shown are starting compositions used by Hammouda (2003) and Thomson *et al.* (2016). CaTs-Enstatite (CaTs-En/cats-en) divides fo-cats-qz into silica-saturated (CaTs-En-Qz; Qtz/qtz/qz/Qz-saturated) and silica-undersaturated (Fo-CaTs-En; qz-undersaturated) parts. Other starting compositions used here (Table 1) are either too lime- or CO_2-rich to be in this projection.

Table 3: Electron microprobe composition (wt%) of a few starting mixtures in the system CMAS-CO_2 used in the present study

Mixture[+]	CaO	MgO	Al_2O_3	SiO_2	CO_2[++]
CB - 1	15.11 (0.27)	14.07 (0.19)	14.31 (0.18)	44.63 (0.64)	11.88
CB - 4	4.12 (0.44)	11.88 (0.27)	13.88 (0.37)	46.19 (0.48)	13.93
CB - 9	13.89 (0.26)	11.47 (0.11)	11.81 (0.30)	46.89 (0.22)	15.94
CB - 10	28.89 (0.48)	15.94 (0.22)	6.58 (0.34)	24.66 (0.29)	23.93
CB - 6	29.07 (0.41)	14.74 (0.37)	7.22 (0.11)	29.08 (0.40)	19.89
CB - 13	30.08 (0.34)	13.04 (0.21)	6.55 (0.39)	29.81 (0.33)	20.52

The analyses are averages of 20 measurements with the electron microprobe. [+] Conditions for these experiments are as follows: CB - 1: 4 GPa, 1500°C, 11 h (run 47) CB - 4: 4.5 GPa, 1600°C, 9 h (run 51) CB - 9: 5 GPa, 1650°C, 7.5 h (run 54) CB - 10: 6 GPa, 1500°C, 12 h (run 62) CB - 6: 6 GPa, 1600°C, 7 h (run 67) CB - 13: 7 GPa, 1500°C, 13 h (run 64) [++]The amount of CO_2 in the fused starting mixture calculated by difference from electron microprobe.

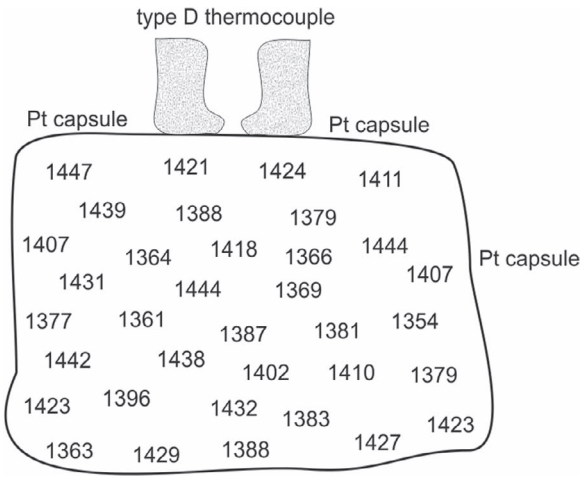

Figure 2. Schematic cross-section of the platinum (Pt) capsule showing the location of temperatures (in °C, numbers inside the Pt capsule), retrieved using microprobe analyses of adjacent opx and cpx, converted from the enstatite-diopside solvus temperature formulation by Gasparik (1990). In this experiment, opx and cpx were initially a 1:1 mixture of end-member enstatite and diopside. This experiment was performed at 5 GPa and 1400°C for approximately 39 h, and this method was used to assess the extent of thermal gradient in the 18/11 type pressure cells with stepped lanthanum chromite heaters as used in the present study. The height and length dimensions of the Pt container in all experiments are approximately 1–1.1 mm and 1.1–1.2 mm, respectively.

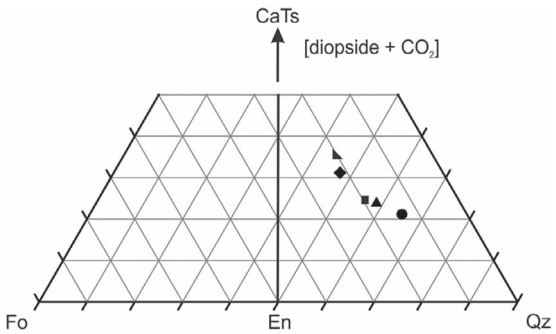

Figure 3. Normative diagram (molecular) with composition of starting mixtures, CB - 1 (filled diamond), CB - 4 (filled, upright triangle), and CB - 9 (filled circle) used at 4, 4.5, and 5 GPa, respectively, in the present study. Also shown are starting compositions, OTBC (filled, right-angled triangle) and ATCM1 (filled square), used in the experimental studies by Hammouda (2003) and Thomson *et al.* (2016), respectively. This diagram is a projection from diopside [di] and carbon dioxide [CO_2] onto the forsterite-calcium tschermak's-quartz (Fo-CaTs-Qz/fo-cats-qz) after Herzberg & O'Hara (1998). Part of the entire CaTs-En line (shown here in thick-solid, inside the trapezium, starting from En/en which is on the fo-qz base) divides the fo-cats-qz join (inside the trapezium) into silica-saturated (Qz/qtz/qz/Qtz/SiO_2-saturated) and silica-undersaturated (qz-undersaturated) parts; the upward-pointing arrow outside the trapezium is in the direction of the CaTs component, and is an extension from the En component. Compositions falling to the right and left of cats-en are silica-saturated and silica-undersaturated, respectively. Starting compositions shown here fall to the silica-rich side of the composition line, CaTs-En. Unless otherwise noted, these mentioned components carry their usual meaning throughout the manuscript.

Experiments were of syntheses type, and hence attainment of chemical equilibrium is not proved. In fact, in these types of experiments, equilibrium is never achieved. For instance, at equilibrium, there would be only grain of each phase (dictated by minimum surface energy) and there would be no thermal gradients. Hence, here it is probably better to make the qualitative statement that equilibrium was approached sufficient for the question being investigated (Table 2).

RESULTS

Experimental conditions are listed in Table 2 and identification of phases was performed on the bases of backscattered electron (BSE) imaging technique and compositions of phases (Tables 3–6). Electron microprobe analyses of the silicate part of some bulk compositions are shown in Table 3, permitting their comparison with the nominal (i.e. prepared before experiments; Table 1) compositions.

In Figs 5–9, BSE images of a few experiments are shown, and Fig. 10 has the coverage of experiments reported here. Except for runs containing only liquid (Table 2; Fig. 10), garnet, coesite, and liquid are always present, regardless of starting compositions. Where there are multiple phases, free vapor is present over the pressure range of 4–5.8 GPa (Table 2; Figs 5–7 and 10).

From 4 to 5 GPa, crystalline phases and liquid are homogeneously distributed in the capsule (Figs 6a, 7, 8). Quenched liquid is both interstitial to crystalline phases and segregated as pools (Fig. 6b). At pressures lower than 5 GPa, liquid quenched to glass (e.g. Figs 5; and 6b), but at higher pressures, it quenched to mixtures of (somewhat) 'glass' and dendrite-type structures (Figs 7–9). Over the pressure range of 4–5.6 GPa, much void space is present, which largely occurs between the capsule wall and crystalline material. This void space, sometimes less than 10 μm across, occurs both near the segregated quenched liquid-crystalline material interface (Fig. 6b), and also much inside the quenched liquid-crystalline material (Fig. 6c). This void space is interpreted to have resulted dominantly from primary carbon dioxide vapor in experiments. While most of the void space is vapor, some of it might also be due either to post-experiment plucking (i.e. falling-out of material) during polishing of experiments, or cracks that came into existence during decompression of pressure cells. Nonetheless, free vapor

Table 4: Electron microprobe analyses (wt%) of crystalline phases and quenched melts from experiments making the two divariant surfaces, vapor + silicate liquid-bearing (4–5 GPa) and dolomite + carbonate liquid-bearing (6–7 GPa), of model carbonated basalt in this study

Experiment	CaO	MgO	Al_2O_3	SiO_2	CO_2	Sum	Ca#$^{++}$
21 (CB - 1)$^{\%}$ – 4 GPa/1250°C/81 h (modally, this experiment has 10 wt% CO_2 vapor)							
Cpx (11)* (10)$^{\&}$	22.57 (0.81)	14.19 (0.77)	11.24 (0.13)	52.49 (0.91)	100.49		
Gt (17) (48)	17.11 (0.79)	16.91 (1.01)	23.64 (0.84)	42.57 (0.61)	100.23		
Cst (7) (8)	0.14 (0.04)	0.08 (0.03)	0.21 (0.04)	99.61 (0.41)	100.04		
Melt (27) (24)	22.43 (1.34)	13.47 (1.21)	11.41 (0.1)	47.18 (1.67)	5.51^{+}	100.00	54.32
X-Cpx^{+++}	XEn: 0.063; XDi: 0.619; XCaTs: 0.149; XCaEs: 0.168	1.000					
X-Gt^{++++}	Si: 2.997; Al: 1.961; Mg: 1.774; Ca: 1.291	8.023					
26 (CB - 1) – 4 GPa/1300oC/77 h (modally, this experiment has 10 wt% CO2 vapor)							
Cpx (13) (22)	21.07 (0.33)	15.12 (0.61)	12.19 (0.09)	51.24 (0.72)	99.62		
Gt (10) (38)	17.21 (0.66) 16.91 (0.49)	23.87 (0.60)	42.26 (0.49)	100.25			
Cst (5) (7)	0.07 (0.02) 0.10 (0.03)	0.10 (0.04)	99.44 (0.61)	99.71			
Melt (31) (23)	23.44 (0.98)	13.61 (1.56)	12.32 (0.18)	44.17 (1.78)	6.46	100.00	55.16
X-Cpx^{+++}	XEn: 0.127; XDi: 0.546; XCaTs: 0.182; XCaEs: 0.145	1.000					
X-Gt^{++++}	Si: 2.977; Al: 1.982; Mg: 1.775; Ca: 1.299	8.032					
37 (CB - 1) – 4 GPa/1350°C/79 h (modally, this experiment has 10 wt% CO_2 vapor)							
Cpx (16) (27)	22.09 (0.59)	14.41 (0.83)	13.78 (0.21)50.11 (0.69)	100.39			
Gt (17) (30)	16.11 (0.79)	17.31 (1.01)	23.22 (0.84)	43.04 (0.61)	99.68		
Cst (5) (7)	0.10 (0.04)	0.14 (0.03)	0.09 (0.03)	99.46 (0.21)	99.79		
Melt (30) (26)	20.94 (1.19)	14.01 (1.39)	14.11 (0.16)	45.21 (1.51)	5.73	100.00	51.63
X-Cpx^{+++}	XEn: 0.105; XDi: 0.550; XCaTs: 0.229; XCaEs: 0.117	1.000					
X-Gt^{++++}	Si: 3.035; Al: 1.930; Mg: 1.819; Ca: 1.217	8.000					
3 (CB - 4) – 4.5 GPa/1300 °C/74 h (modally, this experiment has 12 wt% CO_2 vapor)							
Cpx (12) (5)	21.19 (0.42)	13.47 (0.58)	13.47 (0.19)	51.89 (0.70)	100.02		
Gt (13) (45)	17.12 (0.36)	16.88 (0.54)	23.22 (0.88)	43.14 (0.49)	100.36		
Cst (8) (14)	0.05 (0.02)	0.05 (0.03)	0.11 (0.03)	98.94 (0.17)	99.15		
Melt (22) (24)	21.47 (1.60)	14.11 (1.89)	12.54 (0.19)	44.41 (2.04)	7.47	100.00	52.08
X-Cpx^{+++}	XEn: 0.093; XDi: 0.520; XCaTs: 0.173; XCaEs: 0.214	1.000					
X-Gt^{++++}	Si: 3.030; Al: 1.923; Mg: 1.767; Ca: 1.289	8.008					
7 (CB - 4) - 4.5 GPa/1350°C/80 h (modally, this experiment has 12 wt% CO_2 vapor)							
Cpx (10) (8)	22.18 (0.42)	13.88 (0.58)	13.56 (0.19)	51.04 (0.70)	100.66		
Gt (12) (39)	16.88 (0.36)	17.19 (0.54)	23.76 (0.88)	42.84 (0.49)	100.67		
Cst (6) (13)	0.10 (0.02)	0.08 (0.03)	0.06 (0.03)	99.17 (0.17)	99.41		
Melt (33) (28)	20.84 (1.17)	14.46 (1.49)	13.49 (0.17)	45.04 (1.73)	6.17	100.00	50.72
X-Cpx^{+++}	XEn: 0.086; XDi: 0.555; XCaTs: 0.204; XCaEs: 0.155	1.000					
X-Gt^{++++}	Si: 2.999; Al: 1.961; Mg: 1.794; Ca: 1.266	8.020					
14 (CB - 4) - 4.5 GPa/1400 °C/74 h (modally, this experiment has 11 wt% CO_2 vapor)							
Cpx (10) (12)	21.12 (0.42)	14.82 (0.58)	14.01 (0.19)	50.51 (0.70)	100.46		
Gt (16) (34)	16.91 (0.36)	17.04 (0.54)	23.68 (0.88)	42.93 (0.49)	100.56		
Cst (5) (13)	0.06 (0.02)	0.08 (0.03)	0.10 (0.03)	99.58 (0.17)	99.82		
Melt (30) (30)	19.77 (1.06)	14.52 (1.11)	13.88 (0.19)	44.83 (2.10)	7.00	100.00	49.30
X-Cpx^{+++}	XEn: 0.136; XDi: 0.506; XCaTs: 0.223; XCaEs: 0.136	1.000					
X-Gt^{++++}	Si: 3.008; Al: 1.956; Mg: 1.780; Ca: 1.270	8.014					
Experiment	CaO	MgO	Al_2O_3	SiO_2	CO_2	Sum	Ca#$^{++}$
39 (CB - 9) - 5 GPa/1350°C/85 h (modally, this experiment has 15 wt% CO_2 vapor)							
Cpx (17) (18)	21.59 (0.42)	14.07 (0.58)	14.22 (0.19)	50.49 (0.70)	100.37		
Gt (14) (33)	17.14 (0.36)	16.87 (0.54)	23.22 (0.88)	43.22 (0.49)	100.45		
Cst (5) (17)	0.06 (0.02)	0.10 (0.03)	0.07 (0.03)	99.61 (0.17)	99.84		

Continued

Table 4: Continued

Experiment	CaO	MgO	Al_2O_3	SiO_2	CO_2	Sum	Ca#$^{++}$
Melt (23) (17)	20.97 (1.06)	14.57 (1.11)	13.19 (0.19)	43.98 (2.10)	7.29	100.00	50.69
X-Cpx^{+++}	XEn: 0.110; XDi: 0.520; XCaTs: 0.220; XCaEs: 0.150	1.000					
X-Gt^{++++}	Si: 3.033; Al: 1.921; Mg: 1.764; Ca: 1.289	8.007					
Cpx (17) (15)	21.42 (0.42)	14.58 (0.58)	14.01 (0.19)	50.28 (0.70)	100.29		
Gt (19) (32)	17.04 (0.36)	17.01 (0.54)	23.29 (0.88)	43.37 (0.49)	100.71		
Cst (5) (17)	0.04 (0.02)	0.08 (0.03)	0.10 (0.03)	99.07 (0.17)	99.29		
Melt (28) (21)	21.27 (1.06)	13.79 (1.11)	13.56 (0.19)	45.18 (2.10)	6.20	100.00	52.42
X-Cpx^{+++}	XEn: 0.124; XDi: 0.519; XCaTs: 0.226; XCaEs: 0.132	1.000					
X-Gt^{++++}	Si: 3.034; Al: 1.921; Mg: 1.774; Ca: 1.277	8.006					
31 (CB - 9) - 5 GPa/1450°C/69 h, 30 min (modally, this experiment has 15 wt% CO_2 vapor)							
Cpx (19) (16)	20.86 (0.42)	14.12 (0.58)	13.44 (0.19)	51.68 (0.70)	100.10		
Gt (16) (30)	17.19 (0.36)	17.04 (0.54)	23.48 (0.88)	42.99 (0.49)	100.70		
Cst (6) (17)	0.08 (0.02)	0.10 (0.03)	0.06 (0.03)	99.77 (0.17)	100.01		
Melt (26) (22)	22.18 (1.06)	15.17 (1.11)	13.69 (0.19)	43.01 (2.10)	5.95	100.00	51.08
X-Cpx^{+++}	XEn: 0.116; XDi: 0.508; XCaTs: 0.182; XCaEs: 0.194	1.000					
X-Gt^{++++}	Si: 3.011; Al: 1.939; Mg: 1.779; Ca: 1.290	8.019					
17 (CB- 10) - 6 GPa/1100 °C/86 h							
Cpx (19) (7)	21.61 (0.42)	13.54 (0.58)	13.68 (0.19)	51.28 (0.70)	100.11		
Gt (21) (23)	16.94 (0.36)	16.71 (0.54)	23.72 (0.88)	42.44 (0.49)	99.81		
Cst (7) (11)	0.06 (0.02)	0.05 (0.03)	0.07 (0.03)	99.38 (0.17)	99.56		
SC (14) (27)	32.48 (0.81)	21.96 (0.73)	0	0	45.46	100.00	51.37
Melt (33) (32)	45.87 (2.31)	14.18 (1.59)	0.49 (0.22)	3.58 (1.93)	35.88	100.00	69.79
X-Cpx^{+++}	XEn: 0.090; XDi: 0.532; XCaTs: 0.191; XCaEs: 0.187	1.000					
X-Gt^{++++}	Si: 2.998; Al: 1.975; Mg: 1.759; Ca: 1.282	8.014					
23 (CB - 6) - 6 GPa/1150 °C/87 h 40 min							
Cpx (21) (11)	21.11 (0.42)	14.91 (0.58)	13.21 (0.19)	51.07 (0.70)	100.30		
Gt (18) (24)	17.21 (0.36)	16.88 (0.54)	23.66 (0.88)	42.94 (0.49)	100.69		
Cst (7) (12)	0.07 (0.02)	0.06 (0.03)	0.09 (0.03)	99.27 (0.17)	99.27		
SC (16) (19)	31.87 (0.81)	22.43 (0.73)	0	0	45.70	100.00	50.36
Melt (31) (34)	44.62 (2.11)	14.93 (1.27)	0.24 (0.09)	2.89 (1.37)	37.32	100.00	68.09
X-Cpx^{+++}	XEn: 0.130; XDi: 0.523; XCaTs: 0.201; XCaEs: 0.146	1.000					
X-Gt^{++++}	Si: 3.008; Al: 1.954; Mg: 1.762; Ca: 1.292	8.015					
12 (CB - 6) - 6 GPa/1200°C/85 h							
Cpx (18) (11)	20.99 (0.42)	14.62 (0.63)	13.59 (0.26)	51.08 (0.57)	100.28		
Gt (18) (26)	17.29 (0.23)	16.93 (0.33)	23.59 (0.79)	43.00 (0.56)	100.81		
Cst (7) (11)	0.09 (0.04)	0.05 (0.03)	0.04 (0.03)	99.29 (0.17)	99.47		
SC (19) (20)	33.73 (0.74)	21.54 (0.68)	0	0	44.73	100.00	52.79
Melt (30) (32)	46.18 (1.41)	13.94 (1.22)	0.31 (0.07)	3.28 (1.78)	36.29	100.00	70.29
X-Cpx^{+++}	XEn: 0.129; XDi: 0.510; XCaTs: 0.202; XCaEs: 0.160	1.000					
X-Gt^{++++}	Si: 3.009; Al: 1.946; Mg: 1.766; Ca: 1.297	8.018					
Experiment	CaO	MgO	Al_2O_3	SiO_2	CO_2	Sum	Ca#$^{++}$
8 (CB- 13) - 7 GPa/1050°C/89 h							
Cpx (19) (19)	21.68 (0.37)	13.67 (0.38)	12.84 (0.29)	51.62 (0.62)	99.81		
Gt (21) (18)	17.19 (0.49)	16.90 (0.21)	23.66 (0.38)	43.01 (0.53)	100.76		
Cst (5) (10)	0.06 (0.02)	0.08 (0.04)	0.08 (0.04)	99.38 (0.19)	99.60		
SC (16) (12)	31.84 (0.61)	22.68 (0.53)	0	0	45.48	100.00	50.07
Melt (27) (41)	44.08 (1.99)	14.68 (1.54)	0.29 (0.13)	4.54 (1.73)	36.41	100.00	68.20
X-Cpx^{+++}	XEn: 0.083; XDi: 0.554; XCaTs: 0.173; XCaEs: 0.189	1.000					
X-Gt^{++++}	Si: 3.010; Al: 1.952; Mg: 1.763; Ca: 1.289	8.014					

Continued

Table 4: Continued

Experiment	CaO	MgO	Al_2O_3	SiO_2	CO_2	Sum	Ca#$^{++}$
19 (CB- 13) - 7 GPa/1100 °C/91 h 40 min							
Cpx (17) (20)	22.01 (0.27)	13.36 (0.41)	12.19 (0.43)	51.91 (0.48)	99.47		
Gt (21) (19)	17.02 (0.39)	16.81 (0.27)	23.49 (0.48)	43.36 (0.46)	100.80		
Cst (5) (10)	0.04 (0.02)	0.06 (0.04)	0.06 (0.02)	99.21 (0.29)	99.37		
SC (14) (10)	33.24 (0.71)	21.29 (0.43)	0	0	45.47	100.00	52.72
Melt (32) (41)	45.16 (1.38)	14.27 (1.37)	0.41 (0.23)	2.59 (1.29)	37.57	100.00	69.33
X-Cpx^{+++}	XEn: 0.062; XDi: 0.583; XCaTs: 0.156; XCaEs: 0.199	1.000					
X-Gt^{++++}	Si: 3.033; Al: 1.937; Mg: 1.753; Ca: 1.276	7.998					
5 (CB- 13) - 7 GPa/1150 °C/84 h							
Cpx (14) (21)	21.96 (0.37)	13.47 (0.51)	12.63 (0.37)	52.18 (0.41)	100.20		
Gt (20) (18)	16.83 (0.32)	16.93 (0.45)	23.16 (0.39)	43.22 (0.41)	100.14		
Cst (7) (10)	0.03 (0.02)	0.08 (0.03)	0.05 (0.02)	99.59 (0.23)	99.59		
SC (17) (10)	34.53 (0.62)	20.82 (0.23)	0	0	44.65	100.00	54.22
Melt (26) (41)	44.76 (1.57)	13.24 (1.66)	0.38 (0.17)	2.17 (0.97)	39.45	100.00	70.71
X-Cpx^{+++}	XEn: 0.070; XDi: 0.567; XCaTs: 0.162; XCaEs: 0.201	1.000					
X-Gt^{++++}	Si: 3.039; Al: 1.920; Mg: 1.774; Ca: 1.268	8.001					

[%]The starting composition used. [*]The number of analyses in first parentheses. [&]The modal proportion of the phase (wt%) in second parentheses. [+]CO_2 in SC and quenched melt calculated by difference. [++]Ca# is Ca/Ca + Mg*100 in molar units. [+++]X-Cpx are end-member compositions (molar) of cpx corresponding to the following: En, enstatite; Di, diopside; CaTs, calcium tschermak's; and CaEs, calcium-Eskola. [++++] X-Gt are cation proportions of silicon (Si), aluminum (Al), Ca, and Mg in garnet on the basis of 12 oxygens. Cpx, clinopyroxene; Gt, garnet; Cst, assigned to coesite (free silica phase); SC, solid carbonate (assigned to dolomite); Melt, quenched melt/quenched liquid/liquid

is required in experiments when phase compositions are mass-balanced against starting mixtures. All the same, it is quite likely that since pressure drops during quenching, the volume fraction of vapor can increase, so the abundance of vapor in the quenched runs can exceed than at synthesis conditions. Although this caveat is important to bear in mind, the internally consistent liquid compositions combined with melting phase relations demonstrate that the effect of such quenching might not be large. In some runs, cpx, as a stable, crystalline phase is absent from the phase assemblage over the pressure range of 4–5 GPa (Fig. 10; Tables 2 and 5).

Even where quenched liquid does form separate pools, it is distributed homogeneously and is about 5–50 μm across in experiments at pressures greater than 5 GPa (Figs 7–9). Vapor is absent at greater than 5.8 GPa, an observation that also finds support when phase compositions are mass-balanced against starting mixtures. At pressure of 5.4 GPa and higher, SC, assigned to dolomite in composition, is a stable, crystalline phase. In general, dolomite grains lack a consistent habit, but they can be prismatic (Fig. 7) and, like other phases, are in direct, physical contact with the quenched liquid and vapor. In some runs at 6 and 7 GPa, dolomite is absent from the phase assemblage (Figs 8 and 10; Tables 2 and 5).

Garnet is generally round in its outline (Figs 5 and 7), but can also be subhedral/hypidiomorphic (Figs 6c and 8). A pure-silica phase, assigned to coesite, has the highest relief (e.g. Figs 5 and 8), occurs as equant-shaped grains (Fig. 6c), and next to dolomite, appears the darkest in back scatter images (Figs 6b-c, 7 and 8). Like cpx and dolomite, garnet and coesite are in direct contact with the quenched liquid, and these two phases can also host each other as inclusions (Figs 7 and 8).

In Table 4, compositions of phases are reported when the phase assemblage consists of cpx + garnet + coesite + vapor + liquid over the pressure range of 4–5 GPa, and cpx + garnet + coesite + dolomite + liquid over the pressure range of 6–7 GPa, and Table 5 has compositions of phases when cpx is absent in experiments. Table 6 shows compositions of phases over the pressure range of 5–6 GPa. Modal abundances of phases were calculated using the methods outlined by Presnall (1986). Vapor, where present, is assumed to be pure CO_2, and though coesite has measured concentrations of components (Tables 4–6) other than silica, here it is treated as a pure phase.

Conditions over which dolomite occurs in experiments here are most consistent with predictions and experiments by Chatterjee *et al.* (1998), Luth (2001), Buob *et al.* (2006), and Hammouda *et al.* (2011) and, for the most recent on this subject, reader is referred to Hammouda *et al.* (2011). More important, however, are the observations that (a) dolomite in this study is the stable, crystalline carbonate phase at pressures greater (over 4–7 GPa) than the pressure conditions over which it occurs in model carbonated peridotite (3–4 GPa) in CMAS-CO_2 (Dalton & Presnall, 1998a), and (b) dolomite and garnet are both stable phases over the entire pressure range of 4–7 GPa in this study. That dolomite is stable up to 7 GPa in a 'basic' system with excess silica, as in here, is significant because magnesite replaces dolomite as the stable, crystalline carbonate phase along the high-pressure solidus of model carbonated peridotite in CMAS-CO_2 at greater than 4 GPa. (Coexistence of dolomite and garnet in this study over 4–7 GPa is also significant because Luth, 1995 had queried their coexistence in excess silica 'basic' system at pressures greater than ~3 GPa. Although going back, still, Luth, 1993 reported experiments where dolomite coexists with cpx, garnet, and coesite at 8 GPa, which is somewhat consistent with the present study (up to 7 GPa).)

Compositions of crystalline phases do not depend on either the pressure–temperature conditions or starting compositions. Among all the phases, clinopyroxene can best be described as a high-alumina diopside, while garnet has approximately equal concentrations of pyrope and grossular components. Due to its alumina, and because it always coexists with garnet and coesite (and liquid), cpx is quite vacancy-rich, seen in its relatively

Table 5: Experimental details and electron microprobe analyses (wt%) of crystalline phases and quenched melts (quenched liquids/liquids/melts) that do not occur on the pressure–temperature divariant solidus surface (see Table 2 and Table 4) of model carbonated basalt in the system CMAS-CO_2 in this study

Experiment	CaO	MgO	Al_2O_3	SiO_2	CO_2	Sum	Ca#$^{++}$
13 (CB - 1)$^{\%}$ – 4 GPa/1200°C/85 h (modally, this experiment has 10 wt% CO_2 vapor)							
Gt (14)* (47)$^{\&}$	16.94 (0.45)	16.96 (0.57)	23.86 (0.44)	42.56 (0.31)	100.32		
Cst (7) (9)	0.08 (0.05)	0.06 (0.02)	0.04 (0.02)	98.95 (0.54)	99.13		
Melt (22) (34)	23.41 (0.66)	13.18 (0.81)	11.09 (0.1)	47.27 (2.03)	5.05^{+}	100.00	55.92
24 (CB - 1) – 4 GPa/1400 °C/81 h (modally, this experiment has 10 wt% CO_2 vapor)							
Gt (10) (54)	17.29 (0.69) 16.90 (0.29)	23.34 (0.61)	43.10 (0.39)	100.63			
Cst (5) (9)	0.04 (0.02) 0.07 (0.03)	0.08 (0.03)	99.41 (0.71)	99.71			
Melt (23) (27)	22.71 (0.77)	14.74 (1.23)	12.41 (0.39)	46.21 (0.97)	3.93	100.00	52.39
35 (CB - 4) – 4.5 GPa/1250°C/82 h 20 min (modally, this experiment has 12 wt% CO_2 vapor)							
Gt (19) (45)	17.30 (0.39)	16.61 (0.24)	23.67 (0.43)	43.02 (0.29)	100.60		
Cst (8) (15)	0.05 (0.02)	0.05 (0.03)	0.11 (0.03)	98.94 (0.17)	99.15		
Melt (24) (28)	20.94 (1.39)	14.27 (1.24)	12.71 (0.77)	44.73 (1.81)	7.35	100.00	51.18
38 (CB - 4) - 4.5 GPa/1450°C/69 h (modally, this experiment has 11 wt% CO_2 vapor)							
Gt (15) (43)	17.06 (0.36)	17.07 (0.54)	23.79 (0.29)	42.91 (0.49)	100.83		
Cst (6) (14)	0.04 (0.02)	0.06 (0.03)	0.09 (0.03)	99.16 (0.17)	99.35		
Melt (25) (32)	19.11 (1.38)	15.44 (1.19)	13.18 (0.61)	45.22 (1.33)	7.05	100.00	46.92
15 (CB - 9) - 5 GPa/1300 °C/77 h (modally, this experiment has 15 wt% CO_2 vapor)							
Gt (14) (37)	17.55 (0.29)	16.46 (0.49)	23.59 (0.36)	42.99 (0.33)	100.59		
Cst (8) (20)	0.09 (0.03)	0.05 (0.02)	0.04 (0.03)	99.57 (0.21)	99.75		
Melt (27) (28)	23.10 (1.16)	14.93 (1.11)	13.52 (0.74)	42.11 (2.10)	6.34	100.00	52.50
4 (CB - 9) - 5 GPa/1500°C/29 h (modally, this experiment has 15 wt% CO_2 vapor)							
Gt (16) (37)	16.84 (0.22)	17.22 (0.38)	23.27 (0.49)	43.66 (0.58)	100.99		
Cst (5) (19)	0.04 (0.02)	0.06 (0.03)	0.08 (0.03)	99.31 (0.22)	99.49		
Melt (20) (29)	23.32 (1.23)	14.76 (0.94)	13.38 (1.29)	43.10 (1.84)	5.44	100.00	53.02
41 (CB- 10) - 6 GPa/1050°C/83 h 10 min							
Cpx (21) (11)	21.18 (0.2)	14.28 (0.49)	12.48 (0.46)	51.28 (0.51)	99.22		
Gt (21) (22)	17.22 (0.28)	17.06 (0.34)	23.44 (0.39)	43.22 (0.55)	100.90		
Cst (9) (9)	0.05 (0.03)	0.06 (0.02)	0.07 (0.03)	99.10 (0.28)	99.28		
Melt (30) (58)	41.76 (1.78)	14.97 (1.52)	0.21 (0.09)	1.79 (0.77)	41.30	100.00	66.58
22 (CB - 6) - 6 GPa/1300 °C/76 h							
Cpx (18) (6)	21.86 (0.35)	15.26 (0.43)	12.17 (0.29)	51.29 (0.46)	100.58		
Gt (18) (29)	17.10 (0.19)	16.77 (0.44)	23.77 (0.51)	42.77 (0.38)	100.41		
Cst (5) (12)	0.04 (0.02)	0.07 (0.03)	0.09 (0.03)	99.37 (0.17)	99.57		
Melt (23) (53)	42.17 (1.33)	16.97 (1.29)	0.46 (0.08)	2.11 (0.76)	38.33	100.00	63.96
11 (CB- 13) - 7 GPa/1000°C/89 h 35 min							
Cpx (24) (19)	21.09 (0.55)	13.87 (0.41)	12.68 (0.39)	51.87 (0.57)	99.51		
Gt (21) (19)	17.13 (0.59)	16.99 (0.31)	23.39 (0.33)	43.16 (0.23)	100.54		
Cst (5) (9)	0.05 (0.02)	0.04 (0.04)	0.07 (0.04)	99.22 (0.19)	99.38		
Melt (37) (53)	43.48 (1.27)	14.11 (1.54)	0.14 (0.04)	4.19 (0.73)	38.08	100.00	68.76
Experiment	CaO	MgO	Al_2O_3	SiO_2	CO_2	Sum	Ca#$^{++}$
44 (CB- 13) - 7 GPa/1200°C/86 h							
Cpx (17) (16)	22.13 (0.37)	14.58 (0.21)	11.94 (0.33)	51.77 (0.58)	100.42		
Gt (23) (19)	17.28 (0.59)	16.76 (0.17)	23.09 (0.33)	43.31 (0.52)	100.44		
Cst (6) (10)	0.04 (0.02)	0.05 (0.02)	0.04 (0.02)	99.22 (0.39)	99.22		
Melt (35) (54)	43.64 (1.69)	13.89 (1.77)	0.56 (0.13)	5.17 (2.11)	36.89	100.00	69.18

Details are as in Table 4.

high concentration of calcium-Eskola (CaEs; $Ca_{0.5}\square_{0.5}AlSi_2O_6$) component, which ranges from about 11 to 21 mol% (Tables 4–6). Coexistence, always, with coesite means that solution of CaEs in cpx, at a fixed pressure–temperature condition, is also the maximum possible because garnet and cpx alone are not sufficient to cause it.

DISCUSSION

Melting phase relations, 4–5 GPa

Melting phase relations involving phase assemblage of cpx + garnet + coesite + vapor + liquid are isobaric univariant at 4, 4.5, and 5 GPa. This means that together this phase assemblage forms a divariant surface over 4–5 GPa, and every experiment containing this phase assemblage exists at a fixed PT point on this surface (Fig. 10). The temperatures, over which this divariant phase assemblage exists, rise steadily and, all along, liquid is CO_2-bearing silicate in its composition (Table 4). The concentration of CO_2 in this liquid is between 5 and 7 wt%, and its molar calcium no. [Ca# 100*(Ca/Ca + Mg)] is between 50 and 55. On the low- and high-temperature sides, this divariant surface is bounded by phase assemblages consisting of garnet + coesite + vapor + liquid, and all-liquid, respectively. Compositions of phases show very little variation regardless of whether or not cpx is present in the experiments (Table 5), and this similarity

Table 6: Electron microprobe analyses (wt%) of crystalline phases and quenched melts from experiments over the 5–6 GPa interval in this study

Experiment	CaO	MgO	Al_2O_3	SiO_2	CO_2	Sum	Ca#$^{++}$
107 (CB - 22) – 5.2 GPa/1250°C/82 h 20 min (modally, this experiment has 18 wt% CO_2 vapor)							
Cpx (12) (14)	21.18 (0.23)	14.39 (0.31)	12.44 (0.19)	52.18 (0.42)	100.19		
Gt (9) (20)	17.02 (0.36) 17.11 (0.49)	23.10 (0.30)	43.17 (0.59)	100.40			
Cst (7) (8)	0.06 (0.03) 0.08 (0.02)	0.11 (0.04)	99.37 (0.41)	99.62			
Melt (26) (40)	43.66 (1.41)	14.42 (1.16)	0.06 (0.02)	1.89 (0.88)	39.96^{+}	100.00	68.38
X-Cpx^{+++}	XEn: 0.107; XDi: 0.541; XCaTs: 0.164; XCaEs: 0.189	1.000					
X-Gt^{++++}	Si: 3.031; Al: 1.912; Mg: 1.790; Ca: 1.280	8.013					
103 (CB - 22)$^{\%}$ – 5.2 GPa/1300 °C/73 h (modally, this experiment has 18 wt% CO_2 vapor)							
Cpx (10)* (11)$^{\&}$	21.29 (0.64)	14.55 (0.58)	12.58 (0.19)	52.16 (0.51)	100.58		
Gt (14) (22)	16.91 (0.22)	17.16 (0.48)	23.28 (0.34)	43.29 (0.52)	100.64		
Cst (5) (8)	0.04 (0.02)	0.10 (0.03)	0.06 (0.02)	99.59 (0.21)	99.79		
Melt (29) (41)	43.94 (1.22)	14.78 (1.32)	0.10 (0.04)	2.37 (1.17)	38.81	100.00	67.98
X-Cpx^{+++}	XEn: 0.110; XDi: 0.540; XCaTs: 0.170; XCaEs: 0.179	1.000					
X-Gt^{++++}	Si: 3.030; Al: 1.921; Mg: 1.790; Ca: 1.268	8.009					
111 (CB - 22) – 5.4 GPa/1200°C/79 h 10 min (modally, this experiment has 18 wt% CO_2 vapor)							
Cpx (14) (14)	21.22 (0.29)	14.41 (0.43)	12.32 (0.21)	52.11 (0.46)	100.06		
Gt (11) (20)	17.06 (0.52)	16.97 (0.64)	23.22 (0.44)	43.20 (0.31)	100.45		
Cst (6) (8)	0.04 (0.02)	0.10 (0.04)	0.10 (0.04)	99.53 (0.41)	99.77		
Melt (28) (40)	42.64 (1.09)	14.60 (1.29)	0.10 (0.04)	2.13 (1.07)	40.53	100.00	67.59
X-Cpx^{+++}	XEn: 0.106; XDi: 0.546; XCaTs: 0.163; XCaEs: 0.186	1.000					
X-Gt^{++++}	Si: 3.031; Al: 1.920; Mg: 1.775; Ca: 1.283	8.009					
122 (CB - 19) – 5.4 GPa/1250°C/77 h 40 min (invariant: cpx + gt + cst + void + sc + liquid)							
Cpx (12) (11)	21.32 (0.22)	14.61 (0.28)	12.66 (0.29)	52.14 (0.30)	100.73		
Gt (11) (22)	16.86 (0.36)	17.01 (0.34)	23.31 (0.36)	43.21 (0.49)	100.39		
Cst (8) (8)	0.03 (0.02)	0.08 (0.03)	0.12 (0.03)	99.21 (0.37)	99.21		
SC (11) (12)	33.01 (0.28)	23.59 (0.31)	0	0	43.40	100.00	49.98
Melt (29) (38)	44.97 (1.20)	14.64 (1.49)	0.19 (0.07)	2.22 (1.04)	37.98	100.00	68.69
X-Cpx^{+++}	XEn: 0.112; XDi: 0.539; XCaTs: 0.174; XCaEs: 0.176	1.000					
X-Gt^{++++}	Si: 3.031; Al: 1.928; Mg: 1.778; Ca: 1.267	8.005					
112 (CB - 22) - 5.5 GPa/1150 °C/77 h (modally, this experiment has 18 wt% CO_2 vapor)							
Cpx (14) (15)	21.30 (0.22)	14.29 (0.48)	12.29 (0.29)	52.11 (0.50)	99.99		
Gt (12) (19)	17.10 (0.46)	16.89 (0.44)	23.14 (0.58)	43.19 (0.49)	100.32		
Cst (5) (8)	0.05 (0.03)	0.04 (0.03)	0.12 (0.05)	99.44 (0.47)	99.44		
Melt (30) (40)	43.18 (1.27)	14.52 (1.19)	0.14 (0.07)	2.29 (1.13)	39.87	100.00	67.99
X-Cpx^{+++}	XEn: 0.101; XDi: 0.550; XCaTs: 0.162; XCaEs: 0.188	1.000					
X-Gt^{++++}	Si: 3.035; Al: 1.916; Mg: 1.769; Ca: 1.287	8.007					
109 (CB - 22) – 5.6 GPa/1100 °C/78 h (modally, this experiment has 18 wt% CO_2 vapor)							
Cpx (12) (14)	21.26 (0.22)	14.31 (0.38)	12.22 (0.39)	52.09 (0.40)	99.88		
Gt (13) (20)	17.16 (0.36)	16.96 (0.44)	23.11 (0.48)	43.20 (0.49)	100.43		
Cst (6) (8)	0.06 (0.04)	0.07 (0.03)	0.10 (0.04)	99.60 (0.37)	99.84		
Melt (29) (40)	43.22 (1.16)	14.31 (1.11)	0.20 (0.07)	2.37 (2.10)	39.90	100.00	68.32
X-Cpx^{+++}	XEn: 0.102; XDi: 0.550; XCaTs: 0.160; XCaEs: 0.188	1.000					
X-Gt^{++++}	Si: 3.031; Al: 1.912; Mg: 1.775; Ca: 1.291	8.011					
Experiment	CaO	MgO	Al_2O_3	SiO_2	CO_2	Sum	Ca#$^{++}$
129 (CB - 19) – 5.6 GPa/1150 °C/73 h (invariant: cpx + gt + cst + void + sc + liquid)							
Cpx (12) (9)	21.28 (0.37)	14.38 (0.41)	12.51 (0.33)	52.20 (0.40)	100.37		
Gt (11) (22)	16.94 (0.42)	17.09 (0.44)	23.24 (0.51)	43.19 (0.33)	100.46		
Cst (5) (8)	0.05 (0.02)	0.04 (0.03)	0.07 (0.03)	99.30 (0.42)	99.46		
SC (13) (12)	33.11 (0.41)	23.37 (0.22)	0	0	43.52	100.00	50.29
Melt (30) (41)	44.11 (1.16)	14.59 (1.22)	0.22 (0.10)	2.45 (1.14)	38.63	100.00	68.35

Continued

Table 6: Continued

Experiment	CaO	MgO	Al_2O_3	SiO_2	CO_2	Sum	Ca#$^{++}$
X-Cpx^{+++}	XEn: 0.105; XDi: 0.542; XCaTs: 0.166; XCaEs: 0.187	1.000					
X-Gt^{++++}	Si: 3.029; Al: 1.921; Mg: 1.786; Ca: 1.273	8.010					
147 (CB - 19) – 5.8 GPa/1100 °C/82 h 10 min (invariant: cpx + gt + cst + void + sc + liquid)							
Cpx (15) (10)	21.49 (0.42)	14.28 (0.34)	12.37 (0.44)	52.11 (0.480)	100.25		
Gt (10) (22)	16.82 (0.39)	17.22 (0.24)	23.30 (0.30)	43.28 (0.43)	100.62		
Cst (7) (8)	0.06 (0.03)	0.10 (0.05)	0.11 (0.04)	99.47 (0.39)	99.47		
SC (16) (12)	33.27 (0.28)	23.49 (0.42)	0	0	43.24	100.00	50.29
Melt (26) (41)	43.97 (1.30)	14.81 (1.19)	0.30 (0.08)	2.18 (1.29)	38.74	100.00	67.95
X-Cpx^{+++}	XEn: 0.098; XDi: 0.554; XCaTs: 0.165; XCaEs: 0.183	1.000					
X-Gt^{++++}	Si: 3.029; Al: 1.922; Mg: 1.796; Ca: 1.261	8.009					
132 (CB- 13) – 5.8 GPa/1150 °C/75 h							
Cpx (14) (21)	21.64 (0.32)	13.72 (0.32)	12.64 (0.30)	52.17 (0.36)	100.17		
Gt (17) (16)	17.08 (0.36)	16.72 (0.44)	23.17 (0.47)	43.11 (0.29)	100.08		
Cst (5) (10)	0.09 (0.03)	0.06 (0.04)	0.12 (0.04)	99.39 (0.35)	99.39		
SC (16) (11)	34.31 (0.41)	23.01 (0.43)	0	0	42.68	100.00	51.75
Melt (31) (42)	43.94 (1.49)	14.29 (1.29)	0.27 (0.11)	1.98 (0.77)	39.52	100.00	69.79
X-Cpx^{+++}	XEn: 0.083; XDi: 0.554; XCaTs: 0.162; XCaEs: 0.200	1.000					
X-Gt^{++++}	Si: 3.036; Al: 1.923; Mg: 1.755; Ca: 1.289	8.003					
130 (CB- 13) – 5.8 GPa/1200°C/72 h 15 min							
Cpx (12) (21)	21.82 (0.46)	13.58 (0.54)	12.77 (0.40)	52.20 (0.28)	100.37		
Gt (15) (17)	16.79 (0.38) 16.88 (0.52)	23.22 (0.34)	43.29 (0.37)	100.18			
Cst (7) (10)	0.05 (0.04)	0.10 (0.05)	0.15 (0.07)	99.44 (0.35)	99.74		
SC (13) (10)	34.48 (0.40)	22.89 (0.38)	0	0	42.63	100.00	51.82
Melt (28) (42)	44.28 (1.35)	13.87 (1.40)	0.74 (0.26)	2.22 (0.84)	38.89	100.00	69.51
X-Cpx^{+++}	XEn: 0.077; XDi: 0.558; XCaTs: 0.164; XCaEs: 0.201	1.000					
X-Gt^{++++}	Si: 3.042; Al: 1.923; Mg: 1.768; Ca: 1.264	7.997					

Details are as in Table 4.

Table 7: Data used in the $CaCO_3$-$MgCO_3$ join melting model and the resulting values for the minimum temperature of melting (Tmin), and the composition of the corresponding liquid (X(Ca)min)

Pressure	$T_{melting}$ ($CaCO_3$)	$T_{melting}$ ($MgCO_3$)	$H_m(CaCO_3)$	$H_m(MgCO_3)$	T_{min}	$X(Ca)_{min}$
GPa	K	K	J / mol	J / mol	K	mol%
Model 1						
3	1860	1863	45 000	45 000	1500	0.50
4	1950	1933	45 000	45 000	1560	0.50
5	1980	2023	45 000	45 000	1593	0.51
6	2000	2083	45 000	45 000	1618	0.53
7	2020	2123	45 000	45 000	1635	0.53
8	2025	2173	45 000	45 000	1651	0.55
Model 2						
3	1860	1863	45 000	45 000	1500	0.50
4	1950	1933	45 000	45 000	1560	0.50
5	1980	2023	45 000	42 500	1583	0.52
6	2000	2083	45 000	40 000	1598	0.55
7	2020	2123	45 000	37 500	1605	0.56
8	2025	2173	45 000	37 000	1608	0.58

Melting points of $CaCO_3$ and $MgCO_3$ endmembers were taken from Li *et al.* (2017) and Katsura & Ito (1990), respectively. Starting values for the enthalpies of melting (Hm) of $CaCO_3$ and $MgCO_3$ (model 1) were determined so that the minimum melting point on the join fits with the value at 6 GPa proposed by Buob *et al.* (2006). For model 1, enthalpy values do not vary with pressure (see text for further discussion of the chosen values). For model 2, melting-enthalpy values of CaCO3 were decreased to satisfy the slope change of CaCO3 at high pressure as documented by Li *et al.* (2017).

in compositions implies that the cpx-bearing divariant surface varies little in temperature and topography across a relatively broad pressure range. Despite this, the divariant nature of melting phase relations makes them, in principle, dependent on starting compositions. As one example, compositions of phases along the 5 GPa isobaric univariance are shown in Fig. 11a.

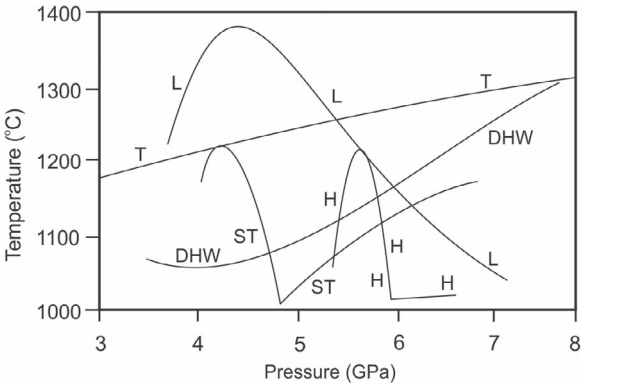

Figure 4. Solidi for carbonate-bearing 'basic' lithologies from various studies. Details are as follows: H, Hammouda (2003; silica-normative starting composition; labeled OTBC); ST, Shirasaka & Takahashi (2003; mid-ocean ridge basalt [MORB] + $CaCO_3$; silica-normative starting composition); DHW, Dasgupta et al. (2004; cpx-garnet cumulate xenolith specimen from Salt Lake Crater, Hawaii; silica-deficient starting composition; labeled SLEC1); L, diopside-CO_2 (Luth, 2006; silica-normative starting composition); and T, Thomson *et al.* (2016; silica-normative starting composition; labeled ATCM1).

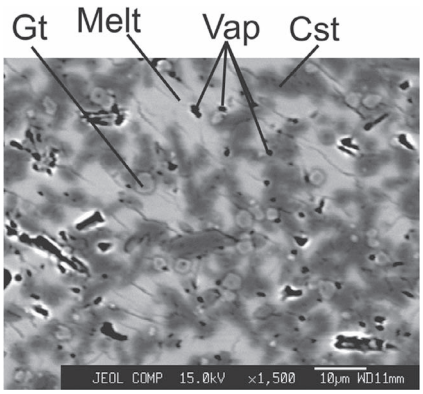

Figure 5. BSE images of experiment 21 (Table 2) at 4 GPa and 1250°C. The phase assemblage consists of clinopyroxene (Cpx/cpx), garnet (Gt/gt), free silica phase assigned to coesite (Cst/cst/coe), vapor (Vap/vap), and quenched melt/quenched liquid/liquid/melt (Melt), with the liquid being CO_2-bearing silicate in its composition (Table 4). This constitutes one of the three runs along isobaric univariance at 4 GPa that contains the same phase assemblage, but at different temperatures. The same phase assemblage also occurs along isobaric univariance at 4.5 and 5 GPa. Here, and from now onward, the position of the type D thermocouple (tungsten-rhenium, $W_{75}Re_{25}/W_{97}/Re_3$) is at the top end in all panels, and in direct with the platinum capsule. The relatively dark areas seen outside some of the capsules shown in all BSE images are the soft alumina and magnesia ceramic inserts in the post-experiment 18/11-type pressure cells. Abbreviations for phases here have the same meaning throughout.

It is not surprising that the high-temperature bounds are all liquid-bearing because, from the sketch in Fig. 1, orthopyroxene (along C-D-H) was (perhaps) never going to be part of the intended phase assemblage. Most likely, however, all-liquid happens because the surface itself is limited, and because of minimal topography along it, starting compositions undergo complete fusion as soon as the surface is breached. Nonetheless, the upper bounds on the divariant surface over 4–5 GPa (Fig. 10) are not very far from those sketched in Fig. 1, indicating that getting guidance from fo-an-di-qz in CMAS (Milholland & Presnall, 1998) had some merit.

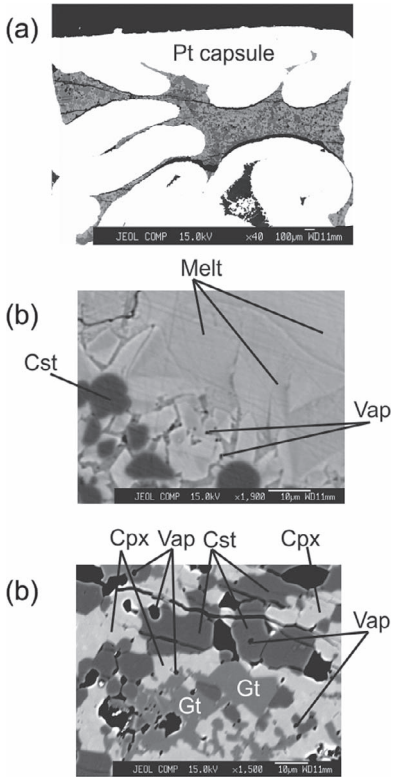

Figure 6. BSE image of experiment 13 (Table 2) at 4 GPa and 1200°C. The phase assemblage consists of garnet (Gt), coesite (Cst), vapor (Vap), and quenched melt (Melt; melt is silicate in its composition). This experiment lacks cpx, and is hence off isobaric univariance at this pressure (Table 5).

Transition from vapor to dolomite, 5–7 GPa

At pressures greater than 5 GPa, different things happened. For example, starting composition CB - 9, used at 5 GPa, produced all-liquid runs at 5.8, 6 and 7 GPa. At both 6 and 7 GPa, a notable feature is the broad temperature interval that have all-liquid runs. These runs, thus, indicate that the opx-and dolomite-bearing univariant curve E, originating from invariance 'f', is either at lower temperatures than estimated in Fig.1, or the more likely possibility is that these starting compositions were unsuitable to intersect the assemblage. The reason for this is that even though the transition from vapor to dolomite was estimated to be between 5 and 6 GPa, it is not guaranteed that the same will happen with the prepared starting compositions. This meant that to get the actual topology, in experiments, at pressures greater than 5 GPa, the most conservative approach was to follow the temperature trajectory almost in a linear fashion using starting compositions used over 4–5 GPa.

Further, it was considered best to have fairly large jumps in pressure after 5 GPa while attempting to locate the transition from vapor to dolomite, and this was done in order to avoid getting lost in composition space. Therefore, pressure was first increased from 5 to 7 GPa, and subsequently lowered to 6 GPa. From all-liquid experiments at 6 and 7 GPa, it became clear that vapor was perhaps no longer part of the phase assemblage, and that dolomite might have replaced it somewhere between 5 and 7 GPa. This also meant that liquid composition may have become carbonate in composition. Accordingly, in order to have dolomite and carbonate liquid in subsequent experiments, while maintaining the rest of the phase assemblage, new starting compositions

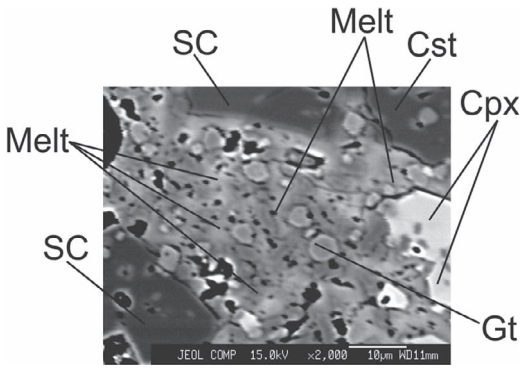

Figure 7. BSE images of experiment 122 (Table 2) at 5.4 GPa and 1250°C. The phase assemblage consists of Cpx + Gt + Cst + Vap + SC + Melt, and is isobaric invariant (six phases). Melt is carbonate in its composition (Table 6), and crystalline carbonate, SC, is assigned to dolomite composition.

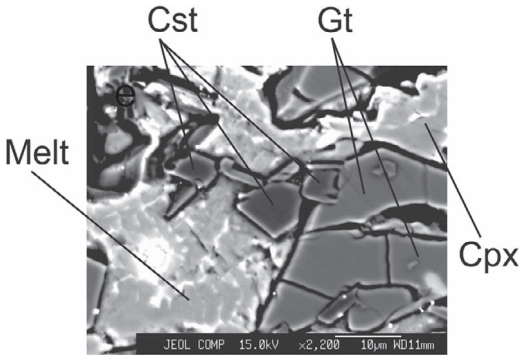

Figure 8. BSE image of experiment 17 (Table 2) at 6 GPa and 1100°C. The phase assemblage consists of Cpx + Gt + Cst + SC + Melt, where melt is carbonate in its composition. This constitutes one of the three runs along isobaric univariance at 6 GPa that contains the same phase assemblage, but different temperatures (Table 4). The same phase assemblage also occurs along isobaric univariance at 5.8 and 7 GPa.

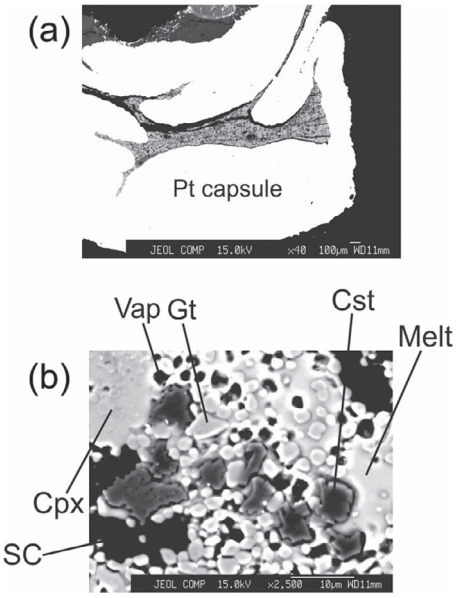

Figure 9. BSE image of experiment 41 (Table 2) at 6 GPa and 1050°C. The phase assemblage lacks SC, and consists of Cpx + Gt + Cst + Melt, and is not along isobaric univariance at this pressure (Table 5). Melt is carbonate in its composition.

were prepared. In fact, as all-liquid runs showed (also discussed later), three different starting compositions, for use at 5.8, 6 and 7 GPa, had to be prepared (Table 1).

Nevertheless, melting phase relations with the phase assemblage of cpx + garnet + coesite + dolomite + liquid are isobaric univariant at 5.8, 6, and 7 GPa. Therefore, this phase assemblage occurs along a divariant surface over 5.8–7 GPa, and every experiment containing it, exists at a fixed PT point on this surface (Fig. 10). As before over 4–5 GPa, the divariant nature of melting phase relations involving dolomite, over 5.8–7 GPa, makes them dependent on starting compositions. The temperatures, over which this divariant phase assemblage exists, decline steadily from 5.8 to 7 GPa and, all along, liquid can best be described as carbonate in its composition (Table 4). The concentration of CO_2 in this liquid is more than 35 wt%, and its molar calcium number is between 67 and 71. Compositions of phases show little variation regardless of whether or not dolomite is present in the experiments (Table 5), and this similarity in compositions implies that the dolomite-bearing divariant surface varies little in temperature and topography with changing pressure. On its low- and high-temperature sides, the surface over 6–7 GPa is bounded by phase assemblages consisting of cpx + garnet + coesite + vapor + liquid and all-liquid, respectively, and the surface itself over 5.8–7 GPa is quite limited in PT space. The temperature bounds on the dolomite-bearing surface here are similar to those reported by Hammouda (2003) and Shirasaka & Takahashi (2003). As one example, compositions of phases along the 6 GPa isobaric univariance are shown in Fig. 11b.

Melting involving five phases in the five-component CMAS-CO_2 is isobaric univariant, and the coefficients of all phases in a balanced equation are meaningful only when the starting composition (bulk) can be shown as a linear, positive combination of these coefficients (Presnall, 1986). Of course, to model partial fusion, a model composition in CMAS-CO_2 must be chosen; a unique method, however, is not available to convert a natural carbonated basalt composition with excess silica into CMAS-CO_2 components, unless components are artificially removed, an exercise that makes the initial, higher variance of fusion of a natural system, tractable. Therefore, in principle, once compositions of all the phases (from the tables here, excluding the liquid), and their modes from various vapor- and dolomite-bearing silicate assemblages from field settings are available, a series of depleted compositions (depleted, because liquid has been extracted) can be prepared. Therefore, to model fusion, any liquid can then be mixed, in any proportion, with the depleted compositions derived earlier, which, in turn, produces an array of bulk compositions (these bulk compositions are, of course, different from those listed in Table 1).

This particular exercise, however, is not possible in this study because modes of vapor- and dolomite-bearing silicate phase assemblages (in basalt) are unknown from field settings. Instead, using compositions and modes of phases from the tables here, average (net) melting reactions (in wt%), using the methods by Presnall (1986) and Walter *et al.* (1995), over 4–5 (silicate liquid-bearing interval, with vapor) and 5.8–7 GPa (carbonate liquid-bearing interval, only with dolomite), are as follows:

4–5 GPa: 0.88 cpx + 0.30 vapor = 0.007 coesite +0.173 garnet +1 liquid

5.8–7 GPa: 2.85 cpx + 2.79 dolomite = 1.56 coesite +3.08 garnet +1 liquid

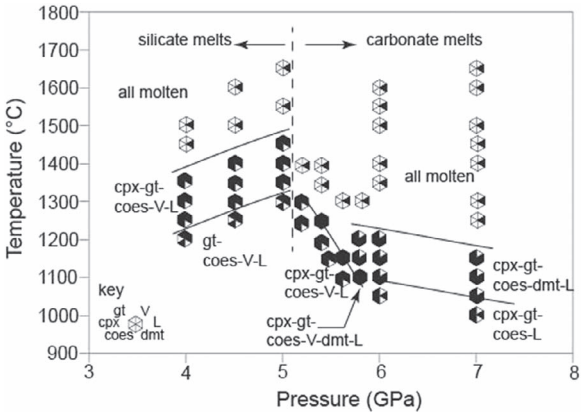

Figure 10. Temperature (T)–pressure (P) plot with experimental conditions of the present study. Key ('key') at the bottom-left in this panel describes the phases that are present in filled. The vertical long-dashed line, between 5 and 5.2 GPa, is drawn to separate the region of silicate melt (to the left of this line) from that of carbonate melt (to the right of this line). The solid lines, containing the areas over 4–5 GPa and 5.8–7 GPa, are divariant surfaces with the phase assemblage of cpx + garnet + coesite + vapor + silicate liquid and cpx + garnet + coesite + dolomite + carbonate liquid, respectively (liquid and coesite are shown as 'L' and 'coes', respectively). The solid curve, over 5.4–5.8 GPa, contains three isobaric invariant points, at 5.4, 5.6, and 5.8 GPa, at each of which, the phase assemblage consists of cpx + garnet + coesite + vapor + dolomite + carbonate liquid. This solid curve corresponds to the solidus ledge of the excess-silica carbonated basalt, which, in turn, is bounded by the two divariant surfaces, by runs over 5.2–5.6 GPa where carbonate liquid coexists with vapor, and by runs that are all molten. Also shown are univariant curves, for dissociation of dolomite, dolomite (dmt) = aragonite (ar) + magnesite (mc), and for carbonation, diopside (di) + CO_2 (vapor/V) = dolomite (dmt) + coesite (coes), from Luth (2001) and Luth (2006), respectively. Curve, dmt = ar + mc, by Luth (2001), is quite similar to that by Chatterjee *et al.* (1998), Buob *et al.* (2006), and Hammouda *et al.* (2011). The most appropriate carbonation reaction, on the basis of Figure 1, in the present study would be, opx + cpx + vapor = garnet + coesite + dolomite. This figure should be read together with Tables 1–6 and, for further details, see 'Results' and 'Discussion' in the main text.

In these reactions, abbreviations take their usual meaning, and because of the very small coefficients of coesite compared with those of the rest of the phases, it could well be on the other side with cpx and vapor over 4–5 GPa. When liquid becomes carbonate in its composition over 5.8–7 GPa, a near doubling of coefficients happens for garnet as compared with coesite, which is required because liquid is extremely poor in alumina and silica.

A "ledge" in carbonated basalt with excess silica

Starting composition CB -13, that gave dolomite-bearing phase assemblage at 7 GPa, produced all-liquid at 5.8 and 5.6 GPa and 1300°C. It was only at 1200°C and 1150°C that the isobaric univariant phase assemblage of cpx + garnet + coesite + dolomite + carbonate liquid was produced, meaning that the dolomite-bearing surface continued down to at least 5.8 GPa (Fig. 10).

With a further decrease in temperature from 1150 to 1100°C at 5.8 GPa, however, both vapor and dolomite are present. This co-occurrence is important because it corresponds to isobaric invariant point at 5.8 GPa and 1100°C, at which the phase assemblage consists of cpx + garnet + coesite + vapor + dolomite + carbonate liquid. This point is bounded, on the 6 GPa side, by the dolomite-present and dolomite-absent runs at 1100 and 1050°C, respectively, and the all-liquid and dolomite-only assemblages at 5.8 GPa (Tables 4–6).

The topology between 5.2 and 5.8 GPa, from the 5 GPa end, was constrained by the following runs: (a) starting composition CB - 9 (used at 5 GPa) had yielded an all-liquid run at 5.2 GPa and 1400°C (Table 2; Fig. 10); (b) likewise, experiments using CB - 9 produced two all-liquid runs at 1400 and 1350°C at 5.4 GPa. These runs were critical because (1) they suggested that the temperatures might not have first decreased between 5 and 5.8 GPa, but somewhere between 5 and 5.2 GPa, and (2) not only could have the transition from vapor to dolomite occurred between 5.2 and 5.8 GPa, other isobaric invariant points, in addition to that at 5.8 GPa/1100°C, may have also existed between 5.2 and 5.8 GPa.

On these bases, a new starting composition, CB - 22, produced a phase assemblage of cpx + garnet + coesite + vapor + carbonate liquid at 5.2, 5.4, 5.5, and 5.6 GPa, but it is only at the 5.2 GPa datum and at temperatures of 1300 and 1250°C that melting phase relations are isobaric univariant. These runs are important because they indicate that, (a) temperatures first decrease between 5 and 5.2 GPa, and not between 5 and 5.8–7 GPa, and (b) liquid is already carbonate in its composition at 5.2 GPa while coexisting with vapor, thus obviating the need to have dolomite to make liquid carbonate in composition. It is because the phase assemblage with carbonate liquid and vapor is identical over 5.2–5.6 GPa (Fig. 11c) that reaction coefficients only at the 5.2 GPa isobaric univariance are shown:

2.27 cpx + 0.9 vapor = 0.79 coesite +1.38 garnet +1 liquid.

When compared with the coefficients over the 4–5 GPa vapor- and silicate liquid-bearing interval, the reaction at 5.2 GPa shows the following: (1) a tremendous increase in the coefficients of cpx, vapor, coesite, and garnet; and (2) the massive contribution of cpx, alone, in making the liquid calcic-carbonate in its composition, which, in turn, makes the relatively high coefficients of coesite and garnet, understandable.

Rather than being pointless, these runs are quite useful. For example, the form of the vapor-, liquid-, and dolomite-only runs between 5 and 5.8 GPa suggests that the dolomite-only surface is narrowing with declining pressure from 7 GPa, and gets terminated by 5.8 GPa, but only toward higher temperatures. These runs also indicate that in order to locate isobaric invariance other than at 5.8 GPa/1100°C, only the starting composition CB - 19 (or something fairly similar to it) might work.

Two more isobaric invariant points occur at 5.6 GPa/1150°C and 5.4 GPa/1250°C, and both have cpx + garnet + coesite + vapor + dolomite + carbonate liquid. Therefore, with three invariant points, melting phase relations are univariant with a negative Clapeyron slope (Fig. 10). The basic chemography at these invariant points does not change much when compared with Fig. 11c, except that dolomite joins the phase assemblage at isobaric invariance (Fig. 11d). The univariant curve with the negative Clapeyron slope corresponds to the solidus 'ledge' of the carbonated basalt with excess silica in this part of the composition space in CMAS-CO_2. Although this ledge, in both its form and position, is very similar to that reported by Hammouda (2003) and Shirasaka & Takahashi (2003), it conflicts with the experimental results reported by Thomson *et al.* (2016) where a ledge is absent over a similar pressure range.

In Fig. 12, compositions of liquids (on CO_2-free bases) are shown that coexist with the following: (1) the five-phase assemblage inclusive of vapor (blank symbols; 4–5 GPa, near the $SiO_2 + Al_2O_3$ apex); (2) the five-phase assemblage inclusive of vapor (shown as 'v', in italics; 5.2–5.6 GPa, near the CaO apex); (3) the six-phase assemblage inclusive of vapor + dolomite (shown as 'i', in italics, filled square; 5.4, 5.6, and 5.8 GPa, near the CaO

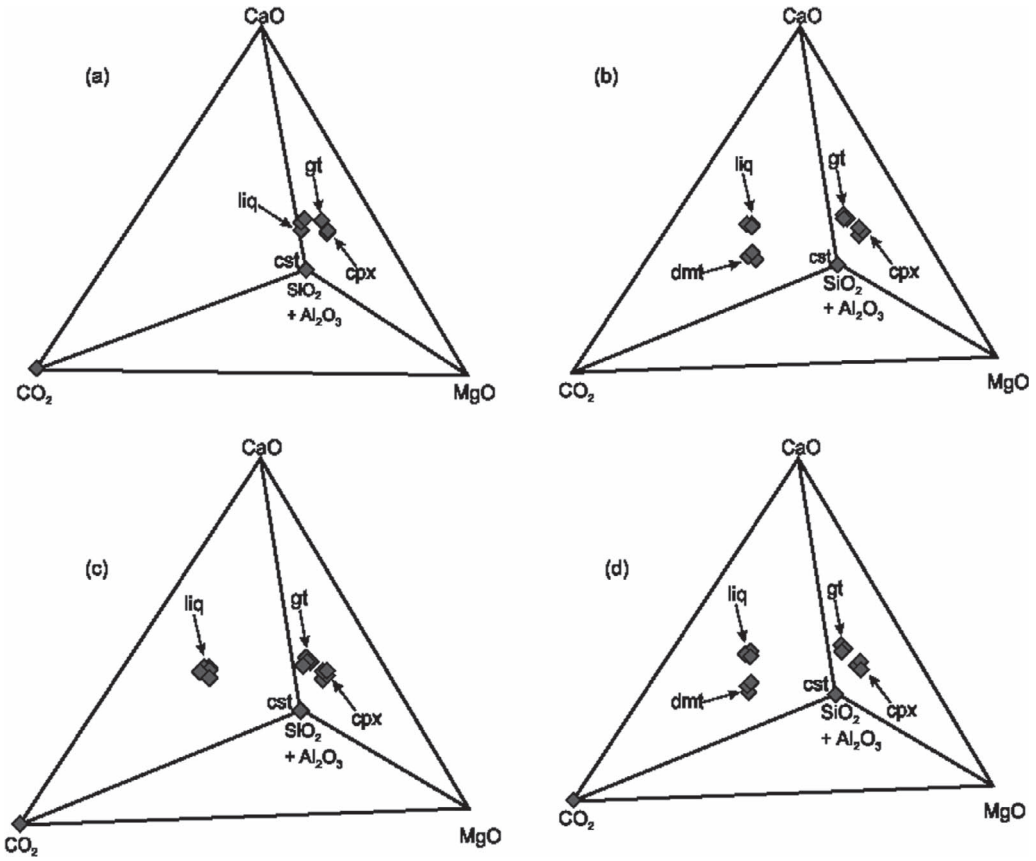

Figure 11. Compositions of all coexisting phases from experiments in this study (a) from the 5 GPa isobaric univariance; (b) from the 6 GPa isobaric univariance; (c) when carbonate liquid coexists with cpx + garnet + coesite + vapor at 5.2, 5.4, 5.5, and 5.6 GPa; (d) the three experiments, at 5.4, 5.6, and 5.8 GPa, that have the isobaric invariant phase assemblage of cpx + garnet + coesite + vapor + dolomite + carbonate liquid. Vapor, at the CO_2 apex, and coesite, at the $SiO_2 + Al_2O_3$ apex, are assumed to be pure phases, and abbreviations are as before.

apex); and (4) the five-phase assemblage inclusive of dolomite (filled circles over 5.8–6 GPa and blank diamonds at 7 GPa, near the CaO apex).

Melting reactions along the univariant solidus ledge

Melting reactions (in wt%), using methods outlined by Presnall (1986), at the three isobaric invariant points are as follows:

5.4 GPa: 5.27 cpx + 0.64 vapor = 2.85 garnet +1.50 coesite +0.85 dolomite +1 liquid.

5.6 GPa: 4.87 cpx + 0.58 vapor = 2.61 garnet +1.39 coesite +0.43 dolomite +1 liquid.

5.8 GPa: 4.37 cpx + 0.53 vapor = 2.30 garnet +1.25 coesite +0.33 dolomite +1 liquid.

Only cpx and vapor contribute toward making liquid, while garnet, coesite, and dolomite are produced. The reaction coefficients of cpx at these points are much higher than those written for the same at the 5.2 GPa datum, and the contribution of cpx and vapor, together with dolomite being produced, could perhaps be understood by considering the following:

(a) along the ledge in model carbonated peridotite in CMAS-CO_2, carbonation, involving liquid and vapor and dolomite, along with forsterite + opx + cpx + garnet, occurs at a fixed point (invariant; say, at ~3 GPa) in pressure–temperature space (Dalton & Presnall, 1998a; also see Novella *et al.*, 2014);

(b) by changing the identity of the phases, invariance (liquid-inclusive) will remain, but the carbonation reaction will change because the (sub-)composition space has now been altered. This, in turn, might reflect the extent (e.g. its length and topology) of a particular ledge in the (new) sub-composition space;

(c) in the present study, carbonation reaction, lacking forsterite but involving opx and free silica and liquid, occurs at a fixed (invariant) point somewhere over 5–6 GPa, which is at a pressure greater than in carbonated peridotite (see Luth, 2006; Hammouda & Keshav, 2015). This implies that the position of carbonation will not change, and that the ledge would be along 'H-f' (Fig. 1). Yet, by not involving opx (from 'f'), variance is gained, necessitating the coexistence of vapor and dolomite and liquid with cpx + garnet + coesite. Thus, the three isobaric invariant points, which together make the univariant solidus ledge here, lie along 'f-g' in the construct in Fig. 1. It is because of this, and also because that dolomite reacts with cpx in making liquid and garnet and coesite along the divariant surface over 5.8–7 GPa, that it is required that only cpx and vapor react along the univariant solidus ledge. An (important) auxiliary benefit of the experimentally determined univariant ledge is that the positions of the rest of the univariant curves, emanating from 'f' (Fig. 1), can be sketched (Fig. 13) with better confidence than would otherwise have been possible, perhaps.

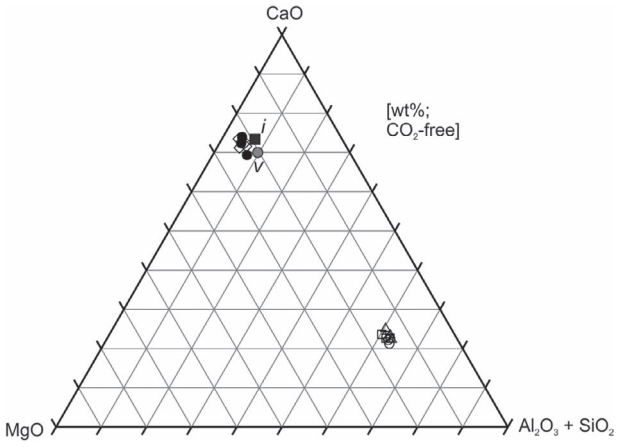

Figure 12. Compositions of liquids (wt%; CO_2-free bases) in experiments from this study over 4–7 GPa. Details are as follows: (a) blank symbols near $Al_2O_3 + SiO_2$ are liquid compositions (silicate) when liquid coexists with cpx + garnet + coesite + vapor, 4–5 GPa; (b) filled circles and blank diamonds near CaO are liquid compositions (carbonate) over 5.8–6 GPa and at 7 GPa, respectively, when liquid coexists with cpx + garnet + coesite + dolomite; (c) filled-gray circles (overlapping) near CaO are liquid compositions (carbonate) when liquid coexists with cpx + garnet + coesite + vapor, over 5.2–5.6 GPa, shown as 'v' in italics here; and (d) filled squares (overlapping) near CaO are liquid compositions (carbonate) when liquid coexists with cpx + garnet + coesite + vapor + dolomite, at the three isobaric invariant points, 5.4, 5.6, and 5.8 GPa, shown as 'i' in italics here.

Although the starting point was melting phase relations in fo-an-di-qz in CMAS, it is curious to see that most of the results here (Fig. 10) conform, more or less, to the sketch in Fig. 1. The ledge in this study not only signifies that the two surfaces, vapor- and dolomite-bearing, merge along it, but also the position of the transition from vapor to dolomite is also precisely known.

Comparison between carbonated basalt with excess silica in this study and carbonated peridotite in CMAS-CO_2 from previous studies

Features observed in carbonate-basalt here have some similarities to those in model carbonated peridotite in CMAS-CO_2. For example, although dolomite is first seen in experiments in model carbonated peridotite at the (~)3 GPa isobaric invariance coexisting with forsterite + opx + cpx + garnet + carbonate liquid, liquid, at the 2.1 GPa isobaric invariance, with forsterite + opx + cpx + spinel + vapor, is already carbonate in its composition—and just at the 1.9 GPa isobaric invariance, liquid, with forsterite + opx + cpx + spinel + vapor, is silicate in composition (with some dissolved CO_2 in it). This indicates that two things must happen to make the liquid calcic-carbonate in its composition: (1) the reaction coefficients of both cpx and vapor, as contributors toward liquid production must be greatly enhanced over this short pressure-distance, i.e. going from 1.9 GPa to 2.1 GPa; and (2) the greatly calcic nature (molar Ca# ~ 67–68) of the liquid at 2.1 GPa can only be accomplished by the massive increase in the coefficients of cpx, for it is the most calcic phase in the entire phase assemblage (e.g. Novella *et al.*, 2014).

To cement these further, one may (re)evaluate the reactions along the univariant solidus of carbonated model peridotite in CMAS-CO_2:

1.7 GPa: 0.30 opx + 0.81 cpx + 0.13 spinel +0.04 vapor = 0.30 forsterite +1 liquid.

1.9 GPa: 0.15 opx + 0.91 cpx + 0.13 spinel +0.04 vapor = 0.24 forsterite +1 liquid.

2.1 GPa: 1.45 forsterite +2.53 cpx + 0.03 spinel +0.42 vapor = 3.43 opx + 1 liquid.

2.9 GPa: 1.25 forsterite +2.45 cpx + 0.10 garnet +0.46 vapor = 3.23 opx + 1 liquid.

3 GPa: 0.90 forsterite +0.16 garnet +2.90 dolomite = 0.56 opx + 0.20 cpx + 1 liquid.

These reactions, over 1.7–1.9 GPa and 2.1–3 GPa with silicate and carbonate liquid, respectively, are along the positive and negative (the ledge) parts of the Clapeyron slope of the solidus, respectively. More significantly, however, these reactions demonstrate the complete dominance of cpx and vapor toward not only the production of liquid but, most crucially, also its composition, and that it is somewhere between 1.9 and 2.1 GPa that the greatest change happens (ignoring the required singularity between 1.9 and 2.1 GPa when forsterite and opx change sides). In model carbonated basalt as inhere, the greatest changes happen between 5 GPa and 5.2 GPa (see before).

The unanswered/unexplained in model carbonated basalt with excess silica in this study, model peridotite carbonated from previous studies, and the system diopside-CO_2

(a) Why do the coefficients of cpx (and vapor) have this massive increase, both in carbonated peridotite and carbonated basalt (here), over a relatively tiny pressure interval of ~0.2 GPa? (b) What is the proper job of dolomite, i.e. beyond its capacity and usefulness to decrease the melting temperature of the prior vapor-bearing silicate phase assemblage in the overall silicate–carbonate mixture? and (c) Is the ∗pull∗ of dolomite from higher pressures so overwhelming that even in its absence, all three, melting phase relations, reaction coefficients, and liquid compositions, change with such sharpness over an interval of 0.2 GPa that the ledge starts to become apparent?

The only other model system study involving cpx + coesite + CO_2 + liquid, via experiments, is diopside-CO_2 from 3 to 8 GPa (Luth, 2006). Compared with the present study, the following features are of note in diopside-CO_2: (a) a ledge is absent (see Fig. 3 in Luth, 2006) and (b) up until the appearance of dolomite at ~5.5 GPa, liquid compositions, including the concentration of the dissolved CO_2 in the liquid, change continuously along the solidus over 3–5.5 GPa (see Table 4 and Figure 11 in Luth, 2006).

Distribution of calcium and magnesium between coexisting dolomite and liquid in carbonate–silicate and carbonate-only mixtures

Figure 14 illustrates the Ca/Mg ratio (expressed as Ca#, Ca/(Ca + Mg)*100, in molar units) of melts and carbonate crystals in equilibrium with each other either along the univariant solidus or in along the divariant surface. The present results at 6 and 7 GPa are plotted as a function of pressure, together with the few data available in the literature in the peridotitic-CO_2 system in CMAS-CO_2 (Dalton & Presnall, 1998a) and in the system diopside-CO_2 (Luth, 2006).

The striking feature of Fig. 14 is the reversal of Ca/Mg partitioning between the peridotitic (ultrabasic) and the eclogitic (basic) systems. This reversal also coincides with a difference in pressure when ultrabasic and basic, silica-saturated systems undergo their respective carbonation reactions. Luth (2006) had commented on the calcic character of the melts in equilibrium with SC on the solidus, and noted that it seemed implausible that the presence of such a tiny amount of silica in the system (i.e. in the liquid)

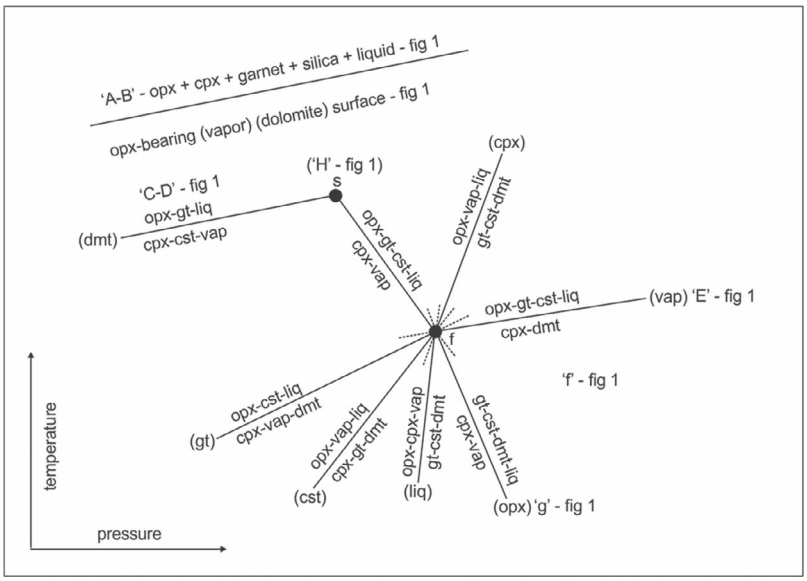

Figure 13. Schreinemakers' construct showing the positions of univariant reactions emanating from invariance 'f' (see Figure 1). The experimentally determined univariant solidus ledge, comprised of three isobaric invariant points at 5.4, 5.6, and 5.8 GPa, in the present study lies along 'f-g' (Figure 1). This construct should be read together with Tables 4–6. Singularity 'H' (Figure 1) in 'Working Method . . . ' in the main text, is shown here as 's'. Abbreviations, for example, opx, are same as before.

could explain this reversal because silica solubility in carbonate melt was exceedingly low.

Focusing on pressure rather than on silica saturation, it can be seen that the reversal occurs between 4 and 6 GPa. One possibility is that the partial molar volumes of melting of $CaCO_3$ and $MgCO_3$ endmember are affected by pressure in a different manner. Recent modeling (Desmaele *et al.*, 2019) indicates that the compressibility curves for the carbonates are different and a reversal of ΔV of melting could explain the present observations on the reversal of Ca/Mg. Recently, Li *et al.* (2017) reported the melting curve of $CaCO_3$ up to 21 GPa in a very detailed manner, wherein the melting curve of $CaCO_3$ had a flattening, and then a slope inversion at ca. 8 GPa, which the authors interpreted as due to density inversion between the coexisting calcite V and liquid. The slope inversion, however, had been interpreted by Hudspeth *et al.* (2018) as being due to the high entropy of calcite V that led to a decrease in the entropy of melting.

Li *et al.* (2017) also compared the melting curves of $CaCO_3$ from their study with that of $MgCO_3$ from Katsura & Ito (1990) up to 15 GPa, and the striking feature was the divergence of the two melting curves from 5 GPa up to higher pressure. On the basis of this divergence, modeling of the evolution of the minimum melting point composition as a function of pressure was performed here. Since the available experimental data are limited (up to 3 GPa: Irving & Wyllie, 1975; at 6 GPa: Buob *et al.*, 2006), here a simple model was built on the basis of the freezing-point depression in the binary system $CaCO_3$-$MgCO_3$.

The freezing-point depression model used here made the assumption of ideal solution in the liquid phase. Given the ionic character of carbonate liquids, this assumption is reasonable, although recent ab initio modeling on the properties of molten carbonates (Hurt & Wolf, 2020) suggest non-ideal mixing of volumes in melts containing $MgCO_3$ at low pressure. The non-ideality decreases as pressure is increased with near-ideal mixing at 12 GPa.

In order to perform the calculation, two approaches were considered for the enthalpies of melting. In the first case, it was assumed that the enthalpies of melting of the $CaCO_3$ and $MgCO_3$ endmembers are equal. Enthalpies of melting of carbonates are not available in the literature but because $CaCO_3$ and $MgCO_3$ have melting temperatures that are quite similar to each other up to 5 GPa. Also, because the minimum melt composition is close to Ca# = 0.5 at low pressure, it was reasonable to assume similar enthalpies of melting. For the purpose of the present modeling, a value of 45 kJ/mol was used. This value is arbitrary but was chosen so that it could reproduce the minimum melting temperature at 6 GPa reported by Buob *et al.* (2006). Note that this value is of the order of the reported low-pressure enthalpies of melting of simple compounds (oxides, sulfides, Robie & Hemingway, 1995). In the second case, equal enthalpies of melting for the endmembers were used only up to 5 GPa. At this pressure, the value for $CaCO_3$ was decreased, to as to take into account the increase in entropy of calcite V, the form of calcite that is present at the solidus at high pressure. An arbitrary value of 2.5 kJ/mol/GPa was chosen, in order to test the effect of the decreasing enthalpy. This value represents about 5% of the starting, low pressure, enthalpy. All values used are summarized in Table 7.

The results of the model are presented in Fig. 15 as tentative liquidus binaries, and no attempt was made to model the subsolidus phase assemblage. In particular, the miscibility gap between magnesite on the Mg-rich side of the diagram and the disordered dolomite/magnesian calcite on the Ca-rich side of the diagram was not treated. The simplified modeling is an attempt to explain the robust observation of the Ca/Mg reversal as reported in Figs 14 and 16 illustrates the evolution of the Ca# of minimum melt as pressure was increased for the two types of dependences of enthalpies on melting of $CaCO_3$ enthalpy of melting dependence. In both cases, the minimum is shifted in the direction of the $CaCO_3$ endmember. The shift is more pronounced when the enthalpy of melting of $CaCO_3$ is allowed to decrease when pressure is increased. As shown schematically in Fig. 15, for a given starting Ca/Mg of the SC (gray vertical stripe in Fig. 15), migration of the minimum composition between the $MgCO_3$ and $CaCO_3$ endmembers may reverse the Ca/Mg crystal/liquid partitioning. For a given value (close to equimolar Ca/Mg, but slightly shifted toward Ca), melts produced at 3 GPa have a Ca/Mg ratio lower than

that of the coexisting SC, whereas melts produced at 8 GPa have a Ca/Mg ratio higher than that of the solid. The pressure at which the crossover takes place depends on the details of the model, such as the dependence of melting temperature on pressure, and the enthalpy of melting.

Therefore, for a starting SC with a given Ca#, there is a possibility for a crossover, in which the minimum melt composition is shifted to the Ca-rich side, causing the reversal of the Ca/Mg partitioning between SC and melt. The reversal is primarily due to the spread between the melting curves of $CaCO_3$ and $MgCO_3$ endmembers above 5 GPa. It may be reinforced by the pressure dependence of the enthalpy of melting of $CaCO_3$. Although Buob *et al.* (2006) did not report on the Ca/Mg inversion on the $CaCO_3$ and $MgCO_3$ binary at 6 GPa, here it is considered that both the modeling and experiments are within small error with each other. Data on the $CaCO_3$ and $MgCO_3$ binary at higher pressures should help in further evaluation of the model presented here. It is also not excluded that more subtle factors could be present, but it appears that the model proposed here captures the essentials of the mechanisms at play.

Further observations on the distribution of calcium and magnesium between coexisting dolomite and carbonate liquid from the present study

Here, in CMAS-CO_2, the following is observed: (a) the liquid is not only more calcic than the coexisting dolomite, but is even more so than in diopside-CO_2 (Fig. 14); (b) every dolomite, coexisting with every liquid, accordingly, is always more magnesian than in diopside-CO_2; (c) if data on the carbonate join are guides, then a liquid this calcic (this study, but also in diopside-CO_2) should coexist with a dolomite that is even more calcic than is actually the case (recap: in model carbonated peridotite in CMAS-CO_2, dolomite is always more calcic than the coexisting liquid, 'obeying' observations made from data on the Ca-Mg carbonate join); (d) melting temperatures, from the 5.4 GPa isobaric invariance to the dolomite-only divariant surface over 5.8–7 GPa, are much lower, by about 200–300°C (Fig. 10), than for minimum melting on the carbonate join (see Fig. 4 in Buob *et al.*, 2006); and (e) thus, the temperatures of minimum melting on the carbonate join are, almost exactly half-way, between the arrival of dolomite in diopside-CO_2 (Luth, 2006) and of the same in the CMAS-CO_2 carbonated basalt in this study (Fig. 10; see Figs 4 and 17 in Buob *et al.*, 2006 and Luth, 2006, respectively).

Possible role of alumina in the distribution of Ca and Mg between coexisting dolomite and liquid

Besides alumina, and hence garnet in the present study, everything else in CMAS-CO_2 is identical with diopside-CO_2—both systems have cpx, vapor, free silica, silicate liquid, carbonate liquid, and dolomite. If anything, with garnet, and because this phase does not take carbon in it, fusion temperatures, including those that characterize the ledge, should not only see an increase than seen here (Fig. 10), but should also move more toward the carbonate join (and by extension, in the direction of melting temperatures as seen in diopside-CO_2). This shift toward higher melting temperatures in the present study must also happen because garnet is a very high temperature-melting silicate, and hence should pull the initial melting of the bulk carbonate-basalt mixture toward higher temperatures, and yet the opposite is observed (melting temperatures decrease in carbonate-basalt in experiments in this study, when compared with diopside-CO_2 and the carbonate join).

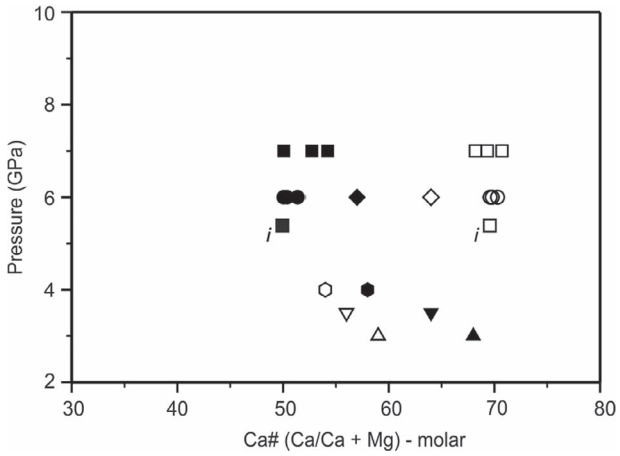

Figure 14. Values of molar Ca# (Ca/Ca + Mg) of the coexisting dolomite (filled symbols) and liquid (blank symbols) as a function of pressure. Details are as follows: (a) circles and squares are along 6 and 7 GPa isobaric univariance, respectively, from the present study; (b) squares with 'i' (in italics) next to them are from the present study at the 5.4 GPa/1250°C isobaric invariance, with the other two isobaric invariant points at 5.6 and 5.8 GPa, also from this study, not shown for clarity; (c) diamonds are data from diopside-CO_2 (Luth, 2006); (d) cross-haired blank diamond (liquid) and cross-haired filled diamond (low-Ca SC) are from diopside-CO_2 (Luth, 2006); and (e) hexagons, inverted triangles, and upright triangles from Dalton & Presnall (1998a) in model carbonated peridotite in the system CMAS-CO_2. Data from the present study should be read together with Tables 2, 4, and 6 and Buob *et al.* (2006). Coexisting SCs and liquids from the experiments by Yaxley & Brey (2004) are not shown, because both are indistinguishable from each other in this projection (also see Figure 16 in Luth, 2006). The composition of minimum melt (Ca# 59) on the Ca-Mg carbonate join at 3 GPa (Irving & Wyllie, 1975), being virtually indistinguishable from the melt at the 3 GPa isobaric invariance in model carbonated peridotite (Dalton & Presnall, 1998a), is not shown. Further, the composition of minimum melt (Ca# 50) on the Ca-Mg carbonate join at 6 GPa by Buob *et al.* (2006) is also not shown because it overlaps the compositions of dolomite from the present study at the same pressure. For further details on Ca-Mg between dolomite and liquid, also see Buob *et al.* (2006) and Luth (2006).

In the absence of dolomite, for example, the fusion curve/surface of a vapor-bearing silicate assemblage, in the overall silicate–carbonate mixture, will continue, undisturbed, with a positive Clapeyron slope. As Luth (2006) remarked that although part of this Ca/Mg reversal between dolomite and liquid, in diopside-CO_2, could be ascribed to the distribution of Ca/Mg between the coexisting cpx, dolomite, and liquid, the extremes of Ca and Mg observed between the coexisting liquid and dolomite were, however, still too great, when compared with what was observed along the carbonate join. With garnet here, and it needs to be repeated, even more severe calcic and magnesian compositions of liquid and dolomite, respectively, are seen (Fig. 14). This is curious also because the compositions of all the crystalline and liquid phases do not vary much over the entire pressure range of 4–7 GPa. Hence, a preferential distribution of Ca/Mg, between the coexisting cpx, garnet, dolomite, and carbonate liquid, does not seem adequate to explain the extreme liquid and crystalline carbonate compositions. Along the same lines, Luth (2006) also found it implausible that silica, as little in its concentrations as reported in the carbonate liquid, could have effected a change so large as to reverse the distribution of Ca/Mg between dolomite and liquid, and the present study supports this unlikelihood (Tables 4 and 6). Therefore, the reason(s) behind as to why (a) either the melting temperatures decrease due to the presence of garnet (see above) or (b) even minor amounts of silica in the liquids cause such

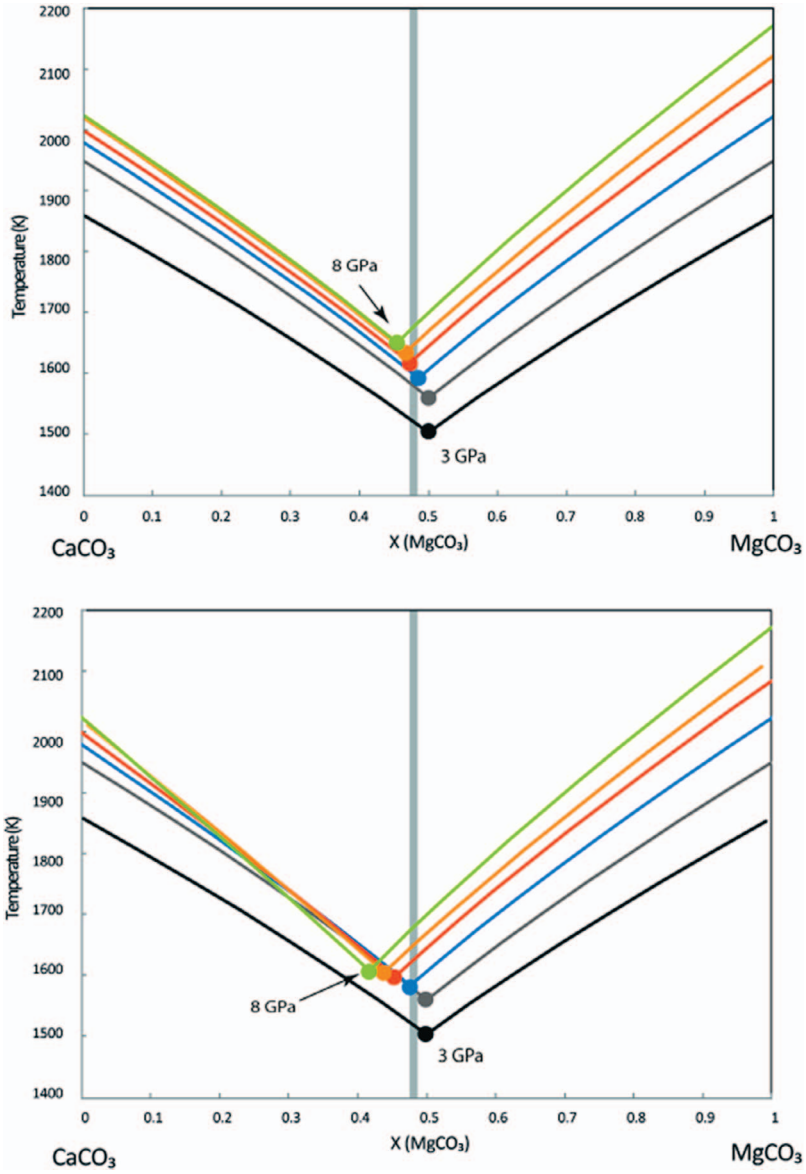

Figure 15. Changes in the position of the composition of minimum melt along the Ca-Mg carbonate join, with the assumption of (panel a) constant enthalpy of fusion of 45 kJ/mol for both $CaCO_3$ and $MgCO_3$; (panel b) constant enthalpy of fusion of 45 kJ/mol for both $CaCO_3$ and $MgCO_3$ up to 5 GPa, and with the value of fusion of enthalpy for $CaCO_3$ decreased to 2.5 kJ/mol at 5 GPa and higher. Number next to a liquidus boundary is pressure in GPa, shown here for data at 3 and 8 GPa, with the rest in sequence between them. See 'Discussion' in the main text for further details.

a tremendous reversal (see above) in the distribution of Ca/Mg between the coexisting dolomite and liquid remain unknown at the moment.

The role of silica-excess on the reversal of Ca and Mg between the coexisting dolomite and liquid

As noted above, Luth (2006) found it implausible that very small amount of silica present in the carbonate melt could cause the observed Ca/Mg partitioning reversal. Silica saturation, however, plays a major role because its presence shifts the carbonation reaction to high pressure.

As Hammouda (2003), the topologies of the peridotite-CO_2 and the eclogite-CO_2 are similar, except that the phase boundaries in the eclogite-CO_2 system are shifted toward high pressures. This shift in the basic system is confirmed in the present study and in Luth (2006). Dasgupta *et al.* (2004) did not find high-pressure carbonation, but this is because in their study a basic, silica-undersaturated, carbonated eclogite composition was used, as described in Hammouda & Keshav (2015).

In the presence of excess silica, olivine (forsterite) is not stable and the carbonation reactions that stabilize the carbonate minerals in the peridotite system (Kushiro *et al.*, 1975; Brey *et al.*, 1983) are suppressed. The next carbonation reaction involves clinopyroxene (Luth, 2001, 2006). A major consequence of this is that the melting reaction that produces carbonatitic melt are shifted to pressure in excess of 4 GPa. According to the model proposed above, the indirect effect of the presence of a silica phase is to cause the reversal of Ca/Mg partitioning by driving the carbonation reaction to higher pressure, compared to the silica-undersaturated system.

In addition, as Hammouda (2003) concludes, and results by Shirasaka & Takahashi (2003) do not change the conclusions, the solidus topology of carbonated peridotite (ultrabasic system) and carbonated basalt (basic system) with excess silica are fairly

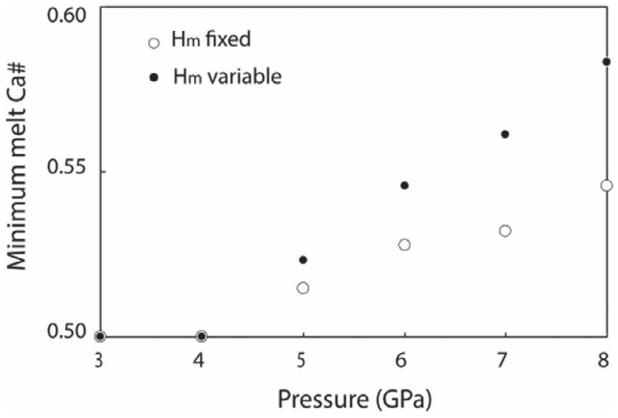

Figure 16. The evolution of the minimum melt Ca# as pressure is increased for the two types of $CaCO_3$ enthalpy of melting dependence.

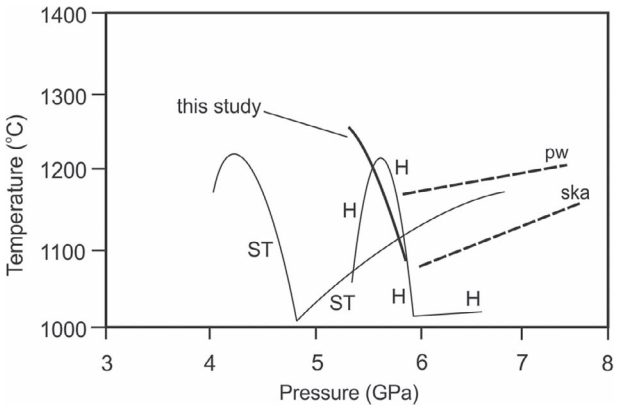

Figure 17. Temperature–pressure diagram showing the univariant solidus ledge of model carbonated basalt with excess silica from this study in CMAS-CO_2, and the solidus curves, including their respective ledge, from studies in natural systems by Hammouda (2003; shown as 'H' here) and Shirasaka & Takahashi (2003; shown as 'ST' here). Modern-day model ocean crust geotherms (Peacock & Wang, 1999, 'pw'; Syracuse *et al.*, 2010, 'ska') are overlaid onto this projection.

similar to each other. The exception is that phase boundaries for carbonation, i.e. the transition from vapor to dolomite, for the latter system are moved toward higher pressure compared with the former system. Carbonation reaction for model peridotite, for example, occurs between 2.5 and 3 GPa and results in a solidus ledge (Hammouda & Keshav, 2015).

Although the reversal in the distribution of Ca/Mg between the coexisting SC and melt might be due to the divergence in the melting curves of $CaCO_3$ and $MgCO_3$ after 5 GPa as described before, it might also be that the direct effects of free silica and garnet, as in this study. Are to physically make a 'more open' and 'more-shifted-toward-calcite' liquid + dolomite divariant loop in basalt-carbonate mixtures (as in this study), possible, than in silica- and alumina-absent Ca-Mg carbonate mixtures (Buob *et al.*, 2006), and also in carbonated peridotite in CMAS-CO2 (Dalton & Presnall, 1998a). This possibility should be considered as a plausible explanation for the observed Ca/Mg reversal between coexisting dolomite and liquid. Such melting-related features, and the possibilities they give forth, are absent in the basalt-carbonate system that lacks excess silica (Dasgupta *et al.*, 2004) and hence, as discussed before, where melting phase relations may be similar to those involving carbonated peridotite.

Application to natural systems

In order to apply the model presented above to natural situations, one missing piece is the actual starting carbonate composition. This depends on the partitioning of Ca and Mg between silicate and carbonate phases present in the subsolidus and on the presence or absence of a vapor phase. In the case of excess CO_2 in the system, Luth (2006) and Martin and Hammouda *et al.* (2011) noted a preferential uptake of Ca in the vapor phase, causing a shift in the residual solid composition toward Mg. On the main question of SC and silicate equilibrium, Hammouda & Keshav (2015) noted that the highly calcic nature of the melts found in the peridotitic system in the 14–20 GPa range could be explained by the stability of majorite at the expense of pyroxene, with majorite favoring Mg over Ca in its crystalline structure. As a consequence, the carbonate and the liquid present at the solidus have more calcium in them.

It is hoped that future work will allow for refining the carbonate–silicate equilibrium Ca/Mg distribution, and that the freezing-point depression model will lead to a better understanding of carbonate–silicate mixtures at elevated pressures, and also such that a generalized picture may also emerge coupling modeling with experiments.

Deep carbon cycle in Earth

It appears that model, modern-day, ocean crust geotherms would intersect the solidus ledge of carbonated basalt at pressures between 5 and 6 GPa (Fig. 17), which correspond to depths of about 150–170 km in Earth. For subducting basaltic crust that passes beyond this intersection, crystalline carbonate, dolomite here, would necessarily melt, effectively removing all carbon from the carbonate–silicate mixture. Therefore, there is very little to suggest anything 'deep' for Earth's carbon cycle purely through the process of subduction. This scenario is very similar to that presented by Hammouda (2003), but is considerably different from that by Dasgupta *et al.* (2004) where the carbon cycle, through subduction, persists to 'great depths' in Earth. The scheme presented here is also considerably different from that presented by Thomson *et al.* (2016) whereby a solidus ledge, over 13–15 GPa, presents an effective barrier for cycling of carbonate, through subduction, much beyond Earth's Transition Zone.

If ancient subducted slabs had temperatures higher (Dasgupta & Hirschmann, 2010) than shown in Fig. 17, then it is most probably that carbonate subduction has been limited throughout the history of Earth. Of course, given the variability of subducting slabs (e.g. Peacock & Wang, 1999; Syracuse *et al.*, 2010), various melting scenarios could be sketched, but the solidus ledge, over the pressure range of 5–6 GPa, ensures that the 'deep' recycling of carbon shall remain confined to depths of less than 200 km in Earth.

Transport of carbon of surface origin to depths greater than ~200 km may happen, as, for example, has been hypothesized for the diamonds bearing eclogite-type inclusions (e.g. Stachel *et al.*, 2004), and for the diamonds containing inclusions of majoritic garnets, and the inclusions whose compositions are largely a combination of calcium, silicon, and oxygen in various proportions (Stachel *et al.*, 2004; Thomson *et al.*, 2016). This situation, however, should be limited to the carbonate located in the coldest parts of the subducted slab, perhaps in deep fractures (Morgan, 2014). Regardless of any of these scenarios, it is more than likely that in terms of global carbon budget, such contributions are, quite possibly, miniscule, and that most of the carbon recycling takes place at depths shallower than 200–250 km in Earth. These limits imply

that alternative explanations, to the very popular idea of attributing recycling of former ocean crust to the origins of a fairly large number of diamonds and their respective guests (e.g. Stachel *et al.*, 2004; Walter *et al.*, 2008; Thomson *et al.*, 2016), are to be sought.

CONCLUSIONS

In the excess-silica model carbonated basalt in the system CaO-MgO-Al_2O_3-SiO_2-CO_2, investigated here between 4 and 7 GPa, the solidus ledge is present, and the topology of the phase relations is very similar to that observed in more complex (natural) carbonate-basalt compositions with excess silica (Hammouda, 2003; Shirasaka & Takahashi, 2003). The pressure range of 5–6 GPa over which the ledge is found in this study is higher by about 2.5–3 GPa than in carbonated ultrabasic system (e.g. carbonated peridotite), confirming the key role played by the free silica phase toward this pressure difference (Hammouda & Keshav, 2015). In attempting to address carbon recycling at Earth's subduction zones, the carbonate solidus ledge over 5–6 GPa acts as a barrier to deep carbonate burial because the ledge is intersected along the pressure–temperature trajectory of the subducted slab, regardless of the thermal regime of subduction (i.e. the age of the slab). This intersection will cause partial fusion, following which, virtually all carbon, from the dolomite in the carbonate–silicate mixture, becomes part of the liquid. Therefore, this partial fusion halts recycling of carbon, with most of it confined to depths less than ~200 km in Earth.

ACKNOWLEDGMENTS

The first author thanks John Brady and S. Anthony (Tony) Morse for exchanges on silicates and carbonates and partial fusion. The authors thank Thomas Sisson and the two anonymous referees for their very helpful and constructive reviews on the work presented here, and editors Reto Gieré and Georg Zellmer for handling the manuscript. The first and third authors thank the administrative and technical colleagues at Bayerisches Geoinstitut, Germany, for their support.

FUNDING

Funding from Bayerisches Geoinstitut, Germany, to the first and third authors, and grant 303301 by the European Union to the first author supported this research. This research was also supported by the French Government Laboratory of Excellence initiative (ANR-10-LABEX-0006, la Région Auvergne, and the European Regional Development Fund. This is Laboratory of Excellence ClerVolc contribution no. 551, Université Clermont-Ferrand, France.

References

Alt, J. & Teagle, D. (1999). The uptake of carbon during alteration of ocean crust. *Geochimica et Cosmochimica Acta* **63**, 1527–1535. https://doi.org/10.1016/S0016-7037(99)00123-4.

Bebout, G. (1995). The impact of subduction-zone metamorphism on mantle-ocean chemical cycling. *Chemical Geology* **126**, 191–218. https://doi.org/10.1016/0009-2541(95)00118-5.

Bohlen, S. R. & Boettcher, A. L. (1982). The quartz-coesite transformation: a precise determination and the effect of other components. *Journal of Geophysical Research* **87**, 7073–7078. https://doi.org/10.1029/JB087iB08p07073.

Bose, K. & Ganguly, J. (1995). Quartz-coesite transition revisited: reversed experimental determination at 500-1200°C and retrieved thermodynamic properties. *American Mineralogist* **80**, 231–238. https://doi.org/10.2138/am-1995-3-404.

Brey, G., Price, W. R., Ellis, D. J., Green, D. H., Harris, K. L. & Ryabchikov, I. D. (1983). Pyroxene-carbonate reactions in the upper mantle. *Earth and Planetary Science Letters* **62**, 63–74.

Buob, A., Luth, R. W., Schmidt, M. W. & Ulmer, P. (2006). Experiments on the $CaCO_3$-$MgCO_3$ solid solutions at high pressure and temperature. *American Mineralogist* **91**, 435–440. https://doi.org/10.2138/am.2006.1910.

Canil, D. & Scarfe, C. (1990). Phase relations in peridotite + CO_2 system to 12 GPa: implications for kimberlites and carbonate stability in the Earth's upper mantle. *Journal of Geophysical Research* **95**, 15805–15816. https://doi.org/10.1029/JB095iB10p15805.

Chatterjee, N., Krueger, R., Haller, G. & Olbricht, W. (1998). The Bayesian approach to an internally consistent thermodynamic database: theory, database, and generation of phase diagrams. *Contributions to Mineralogy and Petrology* **133**, 149–168. https://doi.org/10.1007/s004100050444.

Coogan, L. A. & Dosso, S. E. (2015). Alteration of ocean crust provides a strong temperature dependent feedback on the geological carbon cycle and is a primary driver of the Sr-isotopic composition of seawater. *Earth and Planetary Science Letters* **415**, 38–46. https://doi.org/10.1016/j.epsl.2015.01.027.

Coogan, L. A. & Gillis, K. M. (2013). Evidence that low-temperature oceanic hydrothermal systems play an important role in the silicate-carbonate weathering cycle and long-term climate regulation. *Geochemistry Geophysics Geosystems* **14**, 1771–1786. https://doi.org/10.1002/ggge.20113.

Dalton, J. A. & Presnall, D. C. (1998a). Carbonatitic melts along the solidus of model lherzolite in the system CaO-MgO-Al_2O_3-SiO_2-CO_2. *Contributions to Mineralogy and Petrology* **131**, 123–135. https://doi.org/10.1007/s004100050383.

Dalton, J. A. & Presnall, D. C. (1998b). The continuum of primary carbonatitic-kimberlitic melt compositions in equilibrium with lherzolite: data from the system CaO-MgO-Al_2O_3-SiO_2-CO_2. *Journal of Petrology* **39**, 1953–1964. https://doi.org/10.1093/petroj/39.11-12.1953

Dasgupta, R. & Hirschmann, M. M. (2010). The deep carbon cycle and melting in Earth's interior. *Earth and Planetary Science Letters* **298**, 1–13. https://doi.org/10.1016/j.epsl.2010.06.039.

Dasgupta, R., Hirschmann, M. M. & Withers, A. C. (2004). Deep global cycling of carbon constrained by the solidus of anhydrous, carbonated eclogite under upper mantle conditions. *Earth and Planetary Science Letters* **227**, 73–85. https://doi.org/10.1016/j.epsl.2004.08.004.

Desmaele, E., Sator, N., Vuilleumier, R. & Guillot, B. (2019). The $MgCO_3$–$CaCO_3$–Li_2CO_3–Na_2CO_3–K_2CO_3 melts: thermodynamics and transport properties by atomistic simulations. *Journal of Chemical Physics* **150**, 214503. https://doi.org/10.1063/1.5099015.

Exley, R. A. & Smith, J. V. (1983). Alkremite, garnetite, and eclogite xenoliths from Bellsbank and Jagersfontein, South Africa. *American Mineralogist* **68**, 512–516.

Gale, A., Dalton, C. A., Langmuir, C. H. & Schilling, J.-G. (2013). The mean composition of ocean ridge basalts. *Geochemistry, Geophysics, Geosystems* **14**. https://doi.org/10.1029/2012GC004334.

Gasparik, T. (1990). A thermodynamic model for the enstatite-diopside join. *American Mineralogist* **75**, 1080–1091.

Gudfinnsson, G. H. & Presnall, D. C. (2005). Continuous gradations among primary carbonatitic, kimberlitic, melilitic, basaltic,

picritic, and komatiitic melts in equilibrium with garnet lherzolite at 3-8 GPa. *Journal of Petrology* **46**, 1645–1659. https://doi.org/10.1093/petrology/egi029.

Hammouda, T. (2003). High pressure melting of carbonated eclogite and experimental constraints on carbon recycling and storage in the mantle. *Earth and Planetary Science Letters* **214**, 357–368. https://doi.org/10.1016/S0012-821X(03)00361-3.

Hammouda, T. & Keshav, S. (2015). Melting in the mantle in the presence of carbon: review of experiments and discussion on the origin of carbonatites. *Chemical Geology* **418**, 171–188. https://doi.org/10.1016/j.chemgeo.2015.05.018.

Hammouda, T., Andrault, D., Koga, K., Katsura, T. & Martin, A. M. (2011). Ordering in double carbonates and implications for processes at subduction zones. *Contributions to Mineralogy and Petrology* **161**, 439–450. https://doi.org/10.1007/s00410-010-0541-z.

Hammouda, T., Manthilake, G., Goncalves, P., Chantel, J., Guignard, J., Crichton, W. & Gaillard, F. (2021). Is there a global carbonate layer in the oceanic mantle? *Geophysical Research Letters* **48**, e2020GL089752. https://doi.org/10.1029/2020GL089752.

Herzberg, C. H. & O'Hara, M. J. (1998). Phase equilibrium constraints on the origin of basalts, picrites, and komatiites. *Earth Science Reviews* **44**, 39–79. https://doi.org/10.1016/S0012-8252(98)00021-X.

Hirschmann, M. M. (2018). Comparative deep-earth volatile cycles: the case for C recycling from exosphere/mantle fractionation of major (H_2O, C, N) volatiles and from H_2O/Ce, CO_2/Ba, and CO_2/Nb exosphere ratios. *Earth and Planetary Science Letters* **502**, 262–273. https://doi.org/10.1016/j.epsl.2018.08.023.

Hudspeth, J., Sanloup, C. & Kono, Y. (2018). Properties of molten $CaCO_3$ at high pressure. *Geochemical Perspective Letters* **7**, 17–21. https://doi.org/10.7185/geochemlet.1813.

Hurt, S. M. & Wolf, A. S. (2020). Anomalous structure of $MgCO_3$ liquid and the buoyancy of carbonatite melts. *Earth and Planetary Science Letters* **531**, 165–180. https://doi.org/10.1016/j.epsl.2019.115927.

Irving, A. J. & Wyllie, P. J. (1975). Subsolidus and melting relationships for calcite, magnesite, and the join $CaCO_3$-$MgCO_3$. *Geochimica et Cosmochimica Acta* **39**, 35–53. https://doi.org/10.1016/0016-7037(75)90183-0.

Katsura, T. & Ito, E. (1990). Melting and subsolidus relations in the $MgSiO_3$-$MgCO_3$ system at high pressures: implications to evolution of the Earth's atmosphere. *Earth and Planetary Science Letters* **99**, 110–117. https://doi.org/10.1016/0012-821X(90)90074-8.

Kelemen, P. B. & Manning, C. (2015). Reevaluating carbon fluxes in subduction zones, what goes down, mostly comes up. *Proceedings of the National Academy of Sciences* **112**, E3997–E4006. https://doi.org/10.1073/pnas.1507889112.

Kelley, K. A., Plank, T., Ludden, J. & Staudigel, H. (2003). Composition of the altered oceanic crust at OPS sites 801 and 1149. *Geochemistry, Geophysics, Geosystems* **4**, 8910. https://doi.org/10.1029/2002GC000435.

Keppler, H. & Frost, D. J. (2005) Introduction to minerals under extreme conditions. In: Miletich R. (ed) *EMU Notes in Mineralogy, 7*. Budapest: Eötvös University Press, pp.1–30, https://doi.org/10.1180/EMU-notes.7.1.

Knoche, R., Sweeney, R. J. & Luth, R. W. (1999). Carbonation and decarbonation of eclogites: the role of garnet. *Contributions to Mineralogy and Petrology* **135**, 332–339. https://doi.org/10.1007/s004100050515.

Kushiro, I., Satake, H. & Akimoto, S. (1975). Carbonate-silicate reactions at high pressures and possible presence of dolomite and magnesite in the upper mantle. *Earth and Planetary Science Letters* **28**, 116–120.

Li, Z., Li, J., Lange, R. A., Liu, J. & Militzer, B. (2017). Determination of calcium carbonate and sodium carbonate melting curves up to Earth's transition zone pressures with implications for the deep carbon cycle. *Earth and Planetary Science Letters* **457**, 395–402. https://doi.org/10.1016/j.epsl.2016.10.027.

Liu, T.-C. & Presnall, D. C. (2000). Liquidus phase relations in the system CaO-MgO-Al_2O_3-SiO_2 at 2.0 GPa: applications to basalt fractionation, eclogites, and igneous sapphirine. *Journal of Petrology* **41**, 3–20. https://doi.org/10.1093/petrology/41.1.3.

Luth, R. W. (1993). Diamonds, eclogites, and the oxidation state of the Earth's mantle. *Science* **261**, 66–68. https://doi.org/10.1126/science.261.5117.66.

Luth (1995). Experimental determination of the reaction dolomite + 2 coesite = diopside + 2 CO_2 to 6 GPa. *Contributions to Mineralogy and Petrology* **122**, 152–158. https://doi.org/10.1007/s004100050118.

Luth, R. W. (2001). Experimental determination of the reaction aragonite + magnesite = dolomite at 5 to 9 GPa. *Contributions to Mineralogy and Petrology* **141**, 222–232. https://doi.org/10.1007/s004100100238.

Luth, R. W. (2006). Experimental study of the $CaMgSi_2O_6$-CO_2 system at 3-8 GPa. *Contributions to Mineralogy and Petrology* **151**, 141–157. https://doi.org/10.1007/s00410-005-0051-6.

Luth, R. W. (2009) *Melting of Carbonated Eclogites*. Davos, Switzerland: Goldschmidt Conference.

Marty, B. & Tolstikhin, I. (1998). CO_2 fluxes from mid-ocean ridges, arcs, and plumes. *Chemical Geology* **145**, 233–248. https://doi.org/10.1016/S0009-2541(97)00145-9.

Milholland, C. S. & Presnall, D. C. (1998). Liquidus phase relations in the CaO-MgO-Al_2O_3-SiO_2 system at 3 GPa: the aluminous-pyroxene thermal divide and high-pressure fractionation of picritic and komatiitic magmas. *Journal of Petrology* **39**, 3–27. https://doi.org/10.1093/petroj/39.1.3.

Morgan, J. P. (2014) The Place of Bend-Fault Carbonation in Earth's Long-Term Global Carbon Cycle. Transactions of the European Geosciences Union, ID 14922.

Nishihara, Y., Matsukage, H. N. & Karato, S.-H. (2006). Effects of metal protection coils on thermocouple EMF in multi-anvil high-pressure experiments. *American Mineralogist* **91**, 111–114.

Novella, D., Keshav, S., Gudfinnsson, G. H. & Ghosh, S. (2014). Melting phase relations of model carbonated peridotite from 2 to 3GPa in the system CaO-MgO-Al_2O_3-SiO_2-CO_2 and further indication of possible unmixing between carbonatite and silicate liquids. *Journal of Geophysical Research* **119**, 2780–2800. https://doi.org/10.1002/2013JB010913.

Ogasawara, Y., Ohta, M., Fukasawa, K., Katayama, I. & Maruyama, S. (2000). Diamond-bearing and diamond-free metacarbonate rocks from Kumdy-Kol in the Kokchetav Massif, northern Kazakhstan. *Island Arc* **9**, 400–416. https://doi.org/10.1046/j.1440-1738.2000.00285.x.

Peacock, S. M. & Wang, K. (1999). Seismic consequences of warm versus cool subduction metamorphism: examples from southwest and Northeast Japan. *Science* **286**, 937–939. https://doi.org/10.1126/science.286.5441.937.

Plank, T. & Langmuir, C. H. (1998). The chemical composition of subducting sediment and its consequences for the crust and mantle. *Chemical Geology* **145**, 325–394. https://doi.org/10.1016/S0009-2541(97)00150-2.

Plank, T. & Manning, C. E. (2019). Subducting carbon. *Nature* **574**, 343–352. https://doi.org/10.1038/s41586-019-1643-z.

Presnall, D. C. (1986). An algebraic method for determining equilibrium crystallization and fusion paths in multicomponent systems. *American Mineralogist* **71**, 1061–1070.

Robie, R. A. & Hemingway, B. S. (1995). Thermodynamic properties of minerals and related substances at 298.15 K and 1 Bar (10^5

Pascals) pressure and at higher temperatures. *United States Geological Survey Bulletin* **2131**, 461.

Schettino, E. & Poli, S. (2020) Carbon in Earth's interior. In: Manning C. E., Lin J.-F. & Mao W. (eds) *Hydrous Carbonatitic Liquids Drive CO_2 Recycling from Subducted Marls and Limestones*. Chapter 18: American Geophysical Union.

Schrauder, M. & Navon, O. (1993). Solid carbon dioxide in a natural diamond. *Nature* **365**, 42–44. https://doi.org/10.1038/365042a0.

Shirasaka, M. & Takahashi, E. (2003) A genesis of carbonatitic melt within subducting oceanic crusts: high-pressure experiments in the system MORB-$CaCO_3$. In: *International Kimberlite Conference*. FLA_0043, Vancouver, British Columbia, Canada.

Shirey, S. B., Cartigny, P., Frost, D. J., Keshav, S., Nestola, F., Nimis, P., Pearson, D. G., Sobolev, N. V. & Walter, M. J. (2013). Diamonds and the geology of mantle carbon. *Reviews in Mineralogy and Geochemistry* **75**, 355–421. https://doi.org/10.2138/rmg.2013.75.12.

Smyth, J., Capuruscio, F. A. & McCormick, T. C. (1989). Mantle eclogites: evidence of igneous fractionation in the mantle. *Earth and Planetary Science Letters* **93**, 133–141. https://doi.org/10.1016/0012-821X(89)90191-X.

Stachel, T., Aulbach, S., Brey, G. P., Harris, J. W., Leost, I., Tappert, R. & Viljoen, K. S. (2004). The trace element composition of silicate inclusions in diamonds: a review. *Lithos* **77**, 1–19. https://doi.org/10.1016/j.lithos.2004.03.027.

Staudigel, H., Hart, S. R., Schmincke, H.-U. & Smith, B. M. (1989). Cretaceous ocean crust at DSDP sites 417 and 418: carbon uptake from weathering versus loss by magmatic outgassing. *Geochimica et Cosmochimica Acta* **53**, 3091–3094. https://doi.org/10.1016/0016-7037(89)90189-0.

Syracuse, E., van Keken, P. E. & Abers, G. A. (2010). The global range of subduction zone thermal models. *Physics of the Earth and Planetary Interiors* **183**, 73–90. https://doi.org/10.1016/j.pepi.2010.02.004.

Thomson, A. R., Walter, M. J., Kohn, S. C. & Brooker, R. A. (2016). Slab melting as a barrier to deep carbon subduction. *Nature* **529**, 76–79. https://doi.org/10.1038/nature16174.

Walter, M. J., Sisson, T. W. & Presnall, D. C. (1995). A mass proportion method for calculating melting reactions and application to melting of model upper mantle lherzolite. *Earth and Planetary Science Letters* **135**, 77–90. https://doi.org/10.1016/0012-821X(95)00148-6.

Walter, M. J., Bulanova, G., Armstrong, L. S., Keshav, S., Blundy, J., Gudfinnsson, G., Lord, O., Lennie, A., Smith, C., Gobbo, L. & EIMF (2008). Primary carbonatite melt from deeply subducted oceanic crust. *Nature* **454**, 622–625. https://doi.org/10.1038/nature07132.

Wyllie, P. J., Huang, W.-L., Otto, J. & Byrnes, A. P. (1983). Carbonation of peridotites and decarbonation of siliceous dolomites represented in the system CaO-MgO-SiO2-CO2 to 30 kbar. *Tectonophysics* **100**, 359–388. https://doi.org/10.1016/0040-1951(83)90194-4.

Yaxley, G. M. & Brey, G. P. (2004). Phase relations of carbonate-bearing eclogite assemblages from 2.5 to 5.5 GPa: implications for petrogenesis of carbonatites. *Contributions to Mineralogy and Petrology* **146**, 606–619. https://doi.org/10.1007/s00410-003-0517-3.

Zhang, R. Y. & Liou, J. G. (1996). Coesite inclusions in dolomite from eclogite in the southern Dabie Mountains, China: significance of carbonate minerals in UHPM rocks. *American Mineralogist* **81**, 181–186. https://doi.org/10.2138/am-1996-1-222.

Zhu, Y. & Ogasawara, Y. (2002). Carbon recycled into deep Earth: evidence from dolomite dissociation in subduction-zone rocks. *Geology* **30**, 947–960. https://doi.org/10.1130/0091-7613(2002)030<0947:CRIDEE>2.0.CO;2.